MECHANISMS AND MECHANICS OF NON-STRUCTURAL ADHESION

by

Charles L. Randow

Thesis submitted to the Faculty of the
Virginia Polytechnic Institute and State University
in partial fulfillment of the requirements for the degree of

MASTER OF SCIENCE
IN
ENGINEERING MECHANICS

APPROVED:

David A. Dillard, Chairman

John G. Dillard

Victor Giurgiutiu

December, 1996
Blacksburg, Virginia

Keywords: Adhesion, Cling, Polymeric Films, Viscoelasticity, Curved Adherends, Pressure Sensitive Adhesives

MECHANISMS AND MECHANICS OF NON-STRUCTURAL ADHESION

By
Charles L. Randow
David A. Dillard, Chairman
Engineering Mechanics

(ABSTRACT)

Two topics dealing with adhesion are addressed: an investigation of the cling of thin polymeric films and an analysis of the effects of viscoelasticity on adhesive systems involving curvature mismatch. The results of an investigation into the mechanisms of adhesion and debonding energy associated with the cling between polymeric films and various substrates is presented first. The thermodynamic work of adhesion, electrostatic attraction, and substrate roughness apparently play significant roles in the cling of a film to a substrate. Peel tests are conducted and strain energy release rates are determined which show different debonding energies for the various film-substrate systems. In the analysis of adhesive systems involving curvature mismatch, the focus of the work is on modeling the bond behavior using the solution to the beam on a viscoelastic foundation problem. In addition, the behavior of the adhesive is modeled with a recursive technique using a stress distribution obtained from the solution to the beam on an elastic foundation problem. Debond rate tests are described and conducted so that experimental results may be compared with analytical results. For both adhesion topics, the mechanisms and mechanics of adhesion are considered and experimental tests are conducted.

Acknowledgments

I would like to thank Dr. David Dillard for the attention and time he has given to me in helping me with this research. Beyond that, I would like to thank him for his guidance during the time that I had the privilege to work as one of his students. I would also like to thank Dr. John Dillard and Dr. Victor Giurgiutiu for their advice and help.

For the project dealing with cling, I also acknowledge the assistance of Dr. Tom Ward, Dr. J.P. Wightman, Dr. William Curtin, and Dr. J.T. Dickinson. I also thank Mr. Tony Williams for all of the time and effort he put into this project.

For the project dealing with curvature mismatch and viscoelasticity, I thank Dr. Roger Marchand, Dr. Werner Kohler, and Dr. Jong Kim for their assistance with the mathematical derivations.

I thank the Center for Adhesive and Sealant Science, the National Science Foundation, the Adhesion and Sealant Council, and Reynolds Corporation for supporting this research.

I would like to acknowledge the help of Mr. Rob Humfeld, Dr. Wilson Tsang, and all of the members of the Adhesion Mechanics Laboratory.

Finally, I thank my family for their support and encouragement. ΧΑΡΙΣ

Table of Contents

List of Tables

List of Figures

1.0 INTRODUCTION

Two topics of adhesion are presented in this work. Chapter 2 consists of an investigation of the cling of thin polymeric films and Chapter 3 presents an analysis of the effects of viscoelasticity on adhesive systems involving curvature mismatch. Although the two topics presented in this thesis are unrelated, a common thread runs through both adhesive problems. For each case, the mechanisms of adhesion as well as the mechanics of the particular bonded system are discussed. In each case, experimental tests are conducted to characterize the adhesive system. Finally, the results of these tests are presented for each topic.

A study of the mechanisms of adhesion accounts for a major part of the work presented in Chapter 2. In this study, an attempt is made to partition the measured energy of debonding a polymer film from a substrate to various adhesive mechanisms including the thermodynamic work of adhesion, electrostatic attraction, plastic dissipation, and viscoelastic dissipation. In addition, various factors affecting adhesion are also discussed, including surface roughness, material transfer, and material polarity.

An understanding of the mechanics of a given adhesively bonded system is critical in understanding or predicting its behavior. In Chapter 2, the fundamental mechanics of the peel test are presented with an analysis of mode mix based on peel angle and a study of plasticity. In Chapter 3, the adhesively bonded system is first modeled with a partial differential equation which is derived by considering a beam on a viscoelastic foundation. A recursive solution is also introduced which makes use of a stress distribution obtained from the beam on elastic foundation solution.

In addition to gaining understanding of the adhesive system behavior, a mechanics analysis is also necessary when experiments are conducted to understand exactly what property is being measured. Peel tests are used for analyzing the film behavior in Chapter 2 of this thesis and debond rate tests are conducted for analyzing adhesive behavior in Chapter 3.

Together the two topics presented in this work, although involving very different material systems, demonstrate the type of approach one takes to investigate an adhesively bonded system. It is apparent that contributions from multiple fields of science and engineering are necessary to understand adhesive bond behavior. With the increasing use of adhesives, the type of analysis presented in this thesis will become increasingly more valuable.

2.0 AN INVESTIGATION OF THE CLING OF THIN POLYMERIC FILMS

Thin polymer films often exhibit weak adhesion when brought into contact with other materials. The primary objective of this work is to gain an understanding about the attraction or cling of these flexible polymeric films to rigid substrates. Cling between film and substrate can be analyzed in terms of a global energy balance approach[1], assigning the total debond energy associated with cling to various attractive mechanisms and factors. The attractive mechanisms associated with cling have been examined for other adhesive problems; in particular, a number of authors have investigated the role of van der Waals and electrostatic attractive forces [2,3,4]. This study examines the role of thermodynamic and electrostatic forces, energy dissipation due to plastic or viscoelastic deformation of the films, material polarity, material transfer, and surface roughness on the observed cling of thin polymeric films to various substrates.

Three polymer films were investigated in this study: plasticized poly(vinyl chloride), low density polyethylene, and plasticized poly(vinylidene chloride). The films are commercially available and are typically used for food packaging. The substrates examined were Pyrex glass, stainless steel, high and low density polyethylene, and polypropylene. The substrates were chosen to be representative of materials often wrapped with these polymer films.

Experiments were conducted to investigate the roles which the attractive mechanisms and factors play in the overall cling of a film to a substrate. Initially, material properties of the films were determined and surface analyses of the substrates were conducted. Contact angle measurements and peel tests were utilized to determine the thermodynamic contribution to the work of adhesion and the fracture energy associated with the separating film-substrate combinations. Conclusions are presented from the results of these investigations regarding the various adhesive mechanisms and the behavior of the various films.

2.1 Previous Work

In considering the phenomenon of cling between two materials, it is useful to employ the classic conservation of energy principle. The amount of cling between two materials, defined as the amount of energy required to separate the two materials from each other, is quantified by utilizing an energy balance approach to examine how the debonding energy is expended. In addition, the contribution of the various attractive mechanisms to the total cling may also be investigated with this methodology. An energy balance equation for the peeling of a thin polymeric film from a substrate is given by

$$\delta W - \delta U = \left[W_a + \Psi_e + \Psi_p + \Psi_{ve}\right]\delta A \qquad (2\text{-}1)$$

where δW is the work input of the system, δU is the stored strain energy, and δA is a unit area. The energy terms expended in the debonding of the film are on the right-hand side of the equation. This energy is associated with the thermodynamic work of adhesion (W_a), electrostatic attractive forces (Ψ_e), and dissipation associated with plastic (Ψ_p) and viscoelastic (Ψ_{ve}) deformation of the film.

2.1.1 Work of Adhesion (W_a)

The work of adhesion is a thermodynamic quantity that describes the work done in bringing together or separating two materials[5]. It is worth noting that van der Waals forces act over distances on the order of 10 nm or less[6]. Although the work associated with peel tests is typically two to three orders of magnitude higher than the thermodynamic work, it is believed that the thermodynamic work of adhesion plays a major role in the total work of separating two materials[3,7]. Since the total energy required to peel polymer films without an adhesive from substrates is small, the work of adhesion may be an even greater contributor to overall adhesion than is typically found in other material systems.

2.1.2 Electrostatic Attraction (Ψ_e)

The role of electrostatic attraction in adhesion has been examined for many systems[2,4,8,9,10,11]. It was quite obvious in preparing the test specimens for this study that electrostatic attractive and repulsive forces were present. The polymer films traveled across large distances to contact other surfaces due to electrostatic attractive forces which act over distances as large as 2 cm or more, orders of magnitude greater than the effective range of

van der Waals forces. It is necessary to consider both how the electrostatic attractive forces develop and how they contribute to adhesion.

An electric field develops when a difference in net charge exists between two materials due to an imbalance between electrons or ions. The charge distribution associated with two materials will generally contribute towards both the attraction and repulsion of the two surfaces. An electric field which develops as a result of contact electrification will contribute only towards the attraction of the two surfaces since the charges are opposite[12].

Although contact electrification between insulators has not been widely studied, it has been suggested that the process is similar to contact electrification between metals and insulators[13]. When two materials are brought into contact, charge is transferred from one to the other. If the materials are separated, an electric field develops across the separation distance as shown in Fig. 2.1. This electric field produces attractive forces between the materials which decrease as the separation distance increases since the materials are of finite dimension. It should be noted that, unlike metals, identical insulating materials may still transfer charge due to patches of varying charge present on the material surface and asymmetry inherently present when two materials are brought into contact[14].

The thickness of the film may also affect the amount of charge transferred since the charge may penetrate into the polymer[15]. The depth of charge penetration is dependent on the material system and the type of contact. Based on the work of Fabish, Saltsburg, and Hair[15], the films studied in this project were all of a thickness greater than charge is capable of penetrating under single contact conditions; therefore the thickness of each of the various films should not limit the amount of charge transferred.

The electric field between two materials remains until the charge is discharged. This will occur when the charge finds a path to ground. For example water could condense from the air and create a path to some grounded source. In this work, a path is created through ions in the air with an ion generator to neutralize the charge on the films and on the substrates prior to contact. It is also possible for the charge to break down in the air[16] or to be neutralized by electron tunneling[17].

The attractive and repulsive components of an electrostatic charge act over large distances. Although the breakdown voltage increases as the separation of two plates increases, the magnitude of the electric field is limited by the distance separating the two surfaces and the environment. The maximum sustainable electric field between two plates decreases as the separation distance between the two surfaces increases due to charge breakdown in air[16]. Because of charge breakdown and increased opportunities for

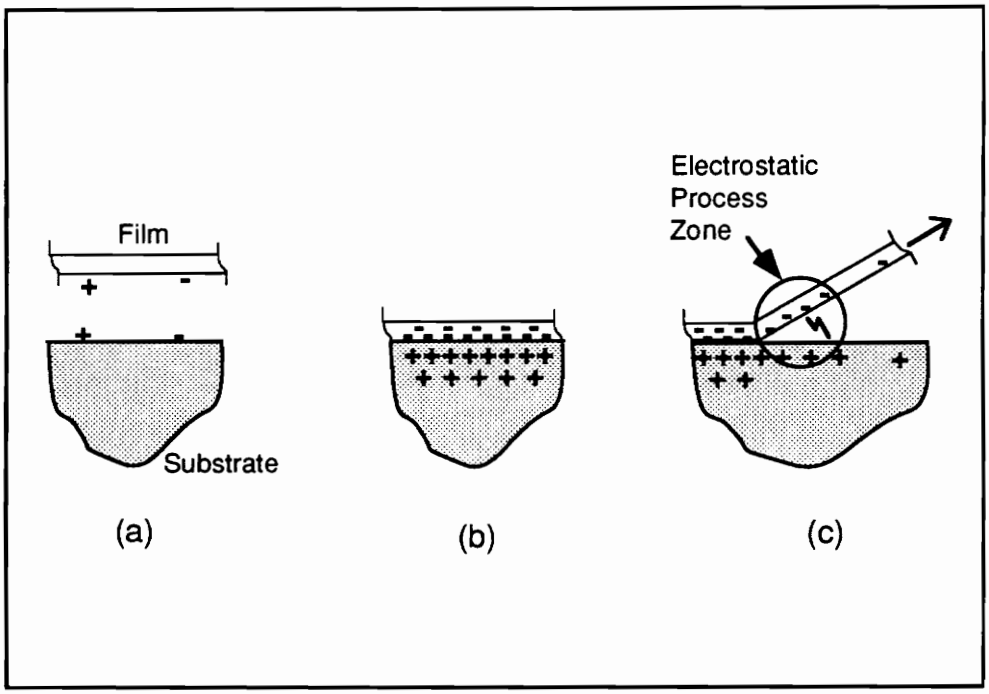

Figure 2.1 - Electrostatic charging before contact of film to substrate (a), during contact (b), and during debonding (c).

dissipation of the charge[2], it is valuable to make a distinction between the effects of electrostatic attraction acting within an electrostatic process zone (located near the crack tip) and acting across the larger separation distances of the post-peel region as shown in Fig. 2.1(c).

2.1.3 Plastic Deformation (Ψ_p)

It is also possible that the films may be undergoing plastic deformation. Since the films are thin (16-21 μm), it is extremely difficult to observe permanent deformation. A ramification of this in the energy balance approach is that a portion of the energy measured in debonding the film from the substrate could actually be dissipated in plastic deformation. This energy would have to be accounted for in the experimentally measured strain energy release rate.

The dissipative component due to plastic deformation during peel tests has been primarily studied for 90° and 180° constant angle tests, assuming elastic-perfectly plastic film behavior[18,19,20,22]. Making use of a non-dimensionalized peel force, η, defined by Kim and Kim[19], the following relation from Thouless and Jensen[20] is rewritten as

$$\eta = \frac{P^2}{E^2 t^2}\left(3\sin^2\theta - \cos^2\theta\right) + \frac{P}{Et}\left[6(1-\cos\theta) + \frac{2\sigma_y}{E}|\cos\theta|\right] \qquad (2\text{-}2)$$

where P refers to the load per unit width, σ_y is the yield strength of the film, t is the film thickness, E is the elastic modulus of the film, and θ is the peel angle. The non-dimensionalized peel force, η, is less than or equal to zero when the film remains elastic and is greater than zero when plastic deformation occurs.

2.1.4 Viscoelastic Effects (Ψ_{ve})

It is theoretically possible to attribute a portion of the debond energy to viscoelastic dissipation if a relationship between peel rate and measured strain energy release rate can be determined. Typically, this phenomenon is due to the time dependency associated with the disentangling of long polymer chains. Although the preliminary results obtained from studying the rate dependency of the three films attached to one of the polymer substrates are presented, a more detailed analysis of the influence of viscoelastic and rate effects is left for future work.

2.1.5 Factors Influencing Cling

In addition to the above mechanisms which contribute to adhesion, a number of factors also play a role in cling by influencing the attractive mechanisms. Both the role of surface roughness and the effect of material transfer have been considered in this work. A correlation between adhesion and the polarity of the various material systems is also suggested. Assessing the contributions to cling of these factors is difficult because they often influence more than one attractive mechanism.

Roughness may be thought of on a variety of scales. In this work, roughness was analyzed over areas of 400 μm^2. Although roughness may also play a role on larger scales, where differences in film rigidity may be significant, this aspect was not considered. When considering a perfectly smooth material, the contact area would equal the total measured area of the contacting materials. Unlike liquids, increasing roughness decreases the contact area since the solid films are unable to conform to the variations in surface topography. Therefore, the energy required to debond a film is modified by the actual area of contact.

Increasing roughness, which leads to decreases in contact area, impacts the thermodynamic forces which are highly dependent on separation distance. Also, since liquids are used in the contact angle experiments which predict the role of thermodynamic forces in cling, the contact angle results must be carefully considered since the films and substrates are solids and contact between the two is not intimate. Roughness also influences electrostatic charging since the electrostatic charge is due primarily to contact electrification when the charge on the films and the substrates is neutralized before contact.

The effect of material transfer between film and substrate was also considered. This transfer results from bringing the two materials into contact. Earlier studies showed material transfer occurring between metal-polymer and polymer-polymer systems[23]. It was shown that the amount of material typically transferred exceeded that necessary to cause the observed contact charging by several orders of magnitude. Subsequent material contact was shown to produce minimal material transfer, although it did produce similar contact charging results. Therefore, it has been suggested that material transfer may only play a secondary role in contact charging[14]. Material transfer may potentially influence the work associated with van der Waals attraction.

The final factor to be considered in the cling of thin polymeric films is the effect of material polarity. The degree of polarity is expressed in terms of the polar contribution to the solubility parameter of each polymer, which is dependent on the side-groups of the

polymer backbone as well as the plasticizer added to the film. This factor may influence the degree to which charge is transferred to the polymer during contact and retained by the polymer during separation. The material polarity is expected to impact the contribution to cling resulting from electrostatic attraction as well as the contribution resulting from thermodynamic forces.

2.2 Experimental Procedures

Three commercially available polymeric films, three polymeric substrates, and two other substrates were considered in these experiments. All are commercially available and are widely used. The films studied were polyethylene (PE film), plasticized poly(vinyl chloride) (PVC film), and plasticized poly(vinylidene chloride) (PVDC film). The three polymer substrates selected were low density polyethylene (LDPE), high density polyethylene (HDPE), and polypropylene (PP). A stainless steel and a Pyrex glass substrate were also included in the experimental system. To analyze the role of surface roughness, three HDPE substrates with varying roughness were utilized.

2.2.1 Surface Energetics and Material Properties

The contribution of the thermodynamic work of adhesion to cling was investigated by using contact angle measurements to analyze surface energies of the various films and substrates. The contact angle of a 5 μL droplet of three probe liquids (water, bromo-napthalene, and formamide) was measured with a goniometer. With knowledge of the surface energies of the probe liquids, the Young-Dupré equation

$$W_a = \gamma_{lv}(1+\cos\varphi) \tag{2-3}$$

was used to determine the work of adhesion, W_a, for each liquid-solid combination, where γ_{lv} refers to the surface free energy at the liquid-vapor interface and φ is the measured contact angle. The spreading pressure is assumed to be negligible. The geometric mean equation

$$W_a = 2\left[\left(\gamma_{lv}^d\gamma_s^d\right)^{1/2} + \left(\gamma_{lv}^p\gamma_s^p\right)^{1/2}\right] \tag{2-4}$$

was used to determine the dispersive and polar components of the surface energy, where the superscripts d and p refer to dispersive and polar, while the subscript s refers to the

solid surface. This is done by rearranging the geometric mean equation into the following form

$$\frac{W_a}{2\left(\gamma_{lv}^d\right)^{1/2}} = \left(\gamma_s^d\right)^{1/2} + \left(\gamma_s^p\right)^{1/2}\left(\frac{\gamma_{lv}^p}{\gamma_{lv}^d}\right)^{1/2} \tag{2-5}$$

and plotting the left-hand side of Eq. 2-5 as a function of $(\gamma_{lv}{}^p/\gamma_{lv}{}^d)^{1/2}$. The data points show a linear relationship and the slope of the line is taken as the square root of the polar component of the solid surface free energy and the intercept as the square root of the dispersive component of the surface free energy[24].

The resulting values of the dispersive and polar components of the surface free energy were combined in the following manner to determine the surface free energy of the material

$$\gamma_s = \gamma_s^d + \gamma_s^p. \tag{2-6}$$

The total thermodynamic work of adhesion, W_a, between two materials is then given by the geometric mean (Eq. 2-4) using the surface free energy values of the film and substrate. It is important to consider that liquid probes were used in determining surface energies experimentally, while in the final system, two solids were placed into contact. Therefore, while liquids have the ability to come into intimate contact with the solid surface, in cases of solid-solid contact, surface roughness plays a critical role in the final contribution of thermodynamic forces to adhesion. The actual thermodynamic work of adhesion is then expected to be less than the predicted value, especially for increasing surface roughness.

The stress-strain behavior of the films was investigated by testing ASTM D-3588 uniaxial dogbone specimens at ambient temperatures. The loading rate was 25 mm per minute. Each film was tested in the machine and transverse directions using a Minimat miniature test frame a minimum of three times.

2.2.2 Peel Testing

A measure of the cling associated with a particular film-substrate combination is the energy required to debond the film from the substrate. From the results of the peel tests, the debonding energy is expressed in terms of a critical strain energy release rate, G_c, which is defined as[22]

$$G_c = \frac{dU_{ext}}{bda} - \frac{dU_s}{bda} - \frac{dU_d}{bda} - \frac{dU_k}{bda} \tag{2-7}$$

where U_{ext} is the external work done, U_s is the strain energy, U_d is the dissipated energy, U_k is the kinetic energy, and *bda* is the fracture area created when the film debonds a length *da* for a width *b*. By assuming the strain energy, the dissipated energy, and the kinetic energy to be negligible, it is possible to rewrite Eq. 2-7 as

$$G_c = P(1-\cos\theta) \tag{2-8}$$

where P is the load per unit width and θ is the angle at which peel occurs[25]. This equation is valid when the material behaves in a linear elastic manner, the substrate is rigid, and the geometry of the region around the crack tip does not change as the film peels. In determining a critical strain energy release rate, both constant angle and constant load experiments were conducted. For the former, a critical debonding load was measured; for the latter, a critical angle at debond was measured.

A constant 90° angle peel testing platform was constructed to be used in an Instron material testing machine as shown schematically in Fig. 2.2(a). These tests were performed under ambient laboratory conditions (60 percent relative humidity and 20° C) at rates which ranged from 0.1 mm/min to 500 mm/min. The load required to cause debonding of the film was used in calculating G_c.

A variable angle peel test was also developed for this study as shown in Fig. 2.2(b). A 4 g mass was attached to the base of the film when the film and substrate were completely vertical (this corresponds to a constant load of 39.4 mN). By using a stirrer motor attached to a series of worm gears, the substrate and film were rotated at an angular rate of 0.7° per second until debonding occurred. The angle at which failure occurred was used in determining G_c. The variable angle peel test is compact and the experiments were conducted in a temperature and humidity controlled chamber, normally at 25 percent relative humidity and 30° C. Tests were conducted at up to 60 percent relative humidity and showed no difference in measured debonding energies.

Before each peel test, the substrates (50 mm wide and 150 mm long) were cleaned with methanol and passed over a volume static eliminator (Chapman VSE 3000) to remove any residual electric charge. The static eliminator produces a balanced mixture of positive and negative ions so that the substrate isolated from ground will not accumulate any net potential greater than 0 ± 5 volts. The film was likewise passed over the static eliminator

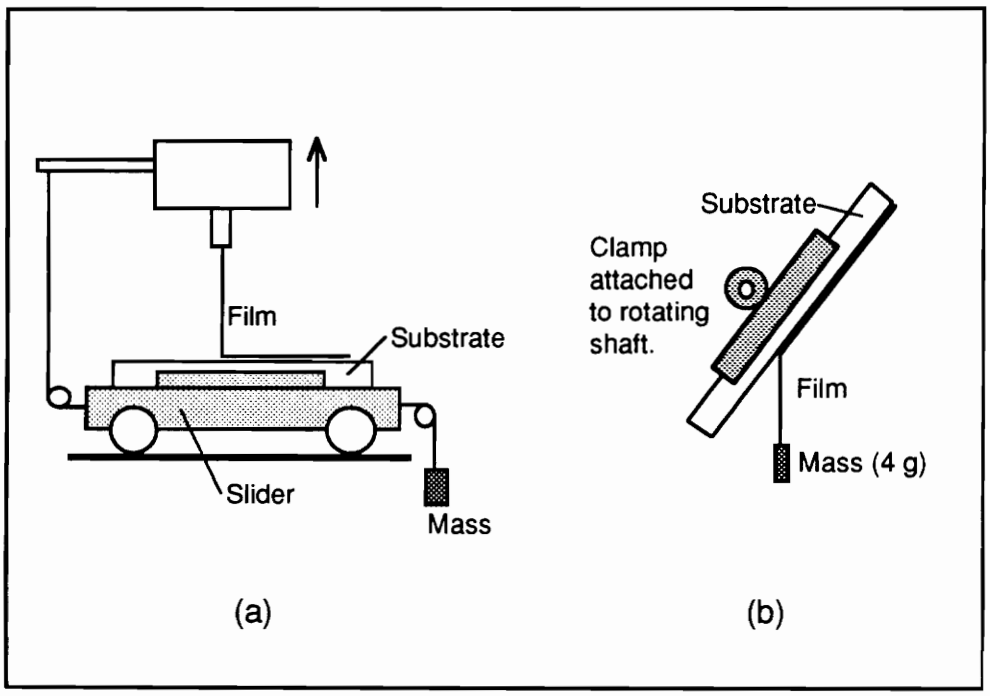

Figure 2.2 - Configuration of the constant 90° angle peel test (a) and the variable angle peel test (b).

before it was applied to the substrate. Any air bubbles in the interface were smoothed out before the load was applied in either test procedure by lightly rubbing the film.

As quickly as possible after the film had debonded from the substrate (within 1-3 seconds) a hand-held electrostatic field meter (Monroe Electronics Stat-Arc Model 255) was used to measure the surface charge density on both the film and the substrate. The residual charge measurement gives an indication about the electric field created between two surfaces as a result of contact electrification, although some charge may well have already dissipated or discharged after debonding occurred. Therefore, the residual charge may be much different that the charge induced by contact electrification.

It is critical to be able to compare strain energy release rates determined for the various tests where peel angles range from less than 20° to greater than 100°. To ensure that the mode mix between mode I and mode II fracture remains nearly identical, the phase angle (Ψ), defined as[20]

$$\Psi = \tan^{-1}\left[\frac{\sqrt{\sin^2\theta + 2(1-\cos\theta)/\varepsilon_\infty} + \tan\omega\cos\theta}{-\tan\omega\sqrt{\sin^2\theta + 2(1-\cos\theta)/\varepsilon_\infty} + \cos\theta}\right], \tag{2-9}$$

was determined for each test, where θ is the peel angle, ω is the angular quantity defined by Suo and Hutchinson[21], and ε_∞ is the applied strain

$$\varepsilon_\infty = \frac{P}{Et}.$$

For this work, ε_∞ was approximately equal to zero. The phase angle is a function of the load, the material properties of both the film and the substrate, the film thickness, and the peel angle. The results of this calculation are presented in Fig. 2.3 for the case of the PE film on the HDPE, glass, and steel substrates. Over the range of peel tests conducted, the phase angle varied between -34° to -38°. Since this variation is small, it is acceptable to make comparisons between the experimentally determined strain energy release rates for the different film-substrate systems. The same conclusion may be drawn for the PVC and PVDC films as well, since there is less mismatch of material properties between those films and the substrates than there is between the PE film and the substrates.

2.2.3 Investigating Electrostatic Attraction

To investigate the effect of electrostatic attractive forces acting over the post-peel region, three peel tests were conducted with varying peel angles and bond widths. Varying

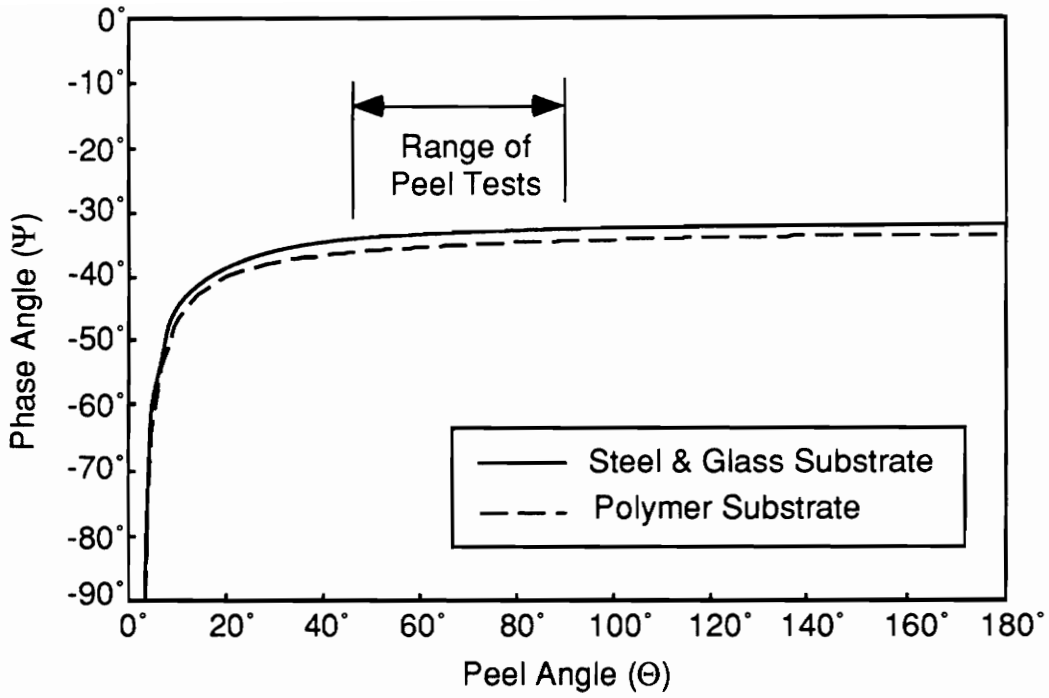

Figure 2.3 - Phase angle as a function of peel angle for the PE film on various substrates.

the bond width was done to highlight the edge effects associated with long-range forces. From fundamental physics, the attraction due to an electric field between two infinite surfaces is independent of the separation distance of those surfaces. Since this is not the case for finite surfaces, changing the surface area is expected to change the attraction between the two surfaces. Different peel angles lead to different separation distances between the substrate and the film as the film is peeling. Therefore, changing the peel angle is also expected to change the attraction between the surfaces. Finally, the free-hanging end of the film that had already debonded during the variable angle peel test was also observed to see if any curvature toward the substrate occurred, an indication of significant long-range attractive forces. As will be mentioned later, no such effects were observed.

To analyze charge transfer, the residual charge on both the film and the substrate was measured after debonding. Since the charge was normally removed before the materials were brought into contact, the remaining charge was due primarily to contact electrification but was mitigated during the peel process. The sensitivity limit on the electrostatic field meter is 10 V/in. The amount of charge transferred was categorized into three general ranges: low charge transfer (less than 0.5 kV/in), intermediate charge transfer (2-5 kV/in), and significant charge transfer (in excess of 5 kV/in). Two peel tests were conducted with films which were not neutralized before contact with the substrate. This procedure gives insight into the difference between the charge due to contact electrification (which produces attractive forces) and the charge inherently present on the film (which produces both attractive and repulsive forces).

2.2.4 Surface Roughness and Material Transfer

Surface roughness was analyzed with an atomic force microscope (Digital Instruments NanoScope III Scanning Probe Microscope) and the topology of sections of the surface area (20 μm by 20 μm) were recorded. Three different methods were used to establish a hierarchy of surface roughness for each of the substrates: the standard deviation of the vertical components of the surface, the mean value of the surface relative to the center plane, and the distribution of the surface area as a function of depth. The first two values are directly obtained from the microscope's analysis package. The last value is obtained by plotting the percentage of the surface which intersects a plane which is lowered into the material surface. Initially, no amount of material intersects the plane. Increasing amounts of the surface intersect the plane as it is lowered into the surface, until the total surface

intersects the plane. The value obtained represents the depth between 10% of the surface and 90% of the surface intersecting the plane. All of the surfaces were used as received, with the exception of the roughened HDPE, which was milled.

To investigate the occurrence of material transfer, X-ray photoelectron spectroscopy (XPS) was utilized to make chemical surface characterization measurements. Experiments were conducted by placing and rubbing the films over both low and high energy substrates. By analyzing the spectra for the individual elements on clean and rubbed surfaces, it is possible to determine the amount and type of material transferred.

2.3 Experimental Results

The results from the experiments investigating the factors influencing cling are presented first so that their influence in surface energy studies and peel tests will be better understood. The standard deviation (R_q), mean value of the surface relative to a center plane (R_a), and the depth of the plane which intersects 10% to 90% of the surface (D) are shown in Table 2.1. The surface roughness experiments show that the glass, stainless steel, LDPE, and HDPE-smooth substrates are the smoothest of the materials. The PP substrate is somewhat rougher and the HDPE-intermediate even rougher still. The HDPE-rough substrate is the roughest of all the materials.

Material transfer results obtained from XPS analysis shows that a significant change in the surface oxygen content occurs on the polymeric substrates after rubbing with the PVC films. It was also observed that the PVC films showed an extremely small transfer of hydrocarbon material to the high surface energy substrates.

An estimate of material polarity was used to rank the polymeric films and substrates by predicting the polar component of the solubility parameter based on the polymer component group contributions[26]. The estimates of polarity for the various polymers suggest that the LDPE, HDPE, and PP substrates show no contribution from a polar component to the solubility parameter (the polar component of the solubility parameter was zero). Therefore, these polymer substrates were classified as exhibiting low polarity. This result was identical for the PE film. Due to the chlorine content of the PVC and PVDC polymer chains and because of the added plasticizer in these materials, these two films exhibited a high degree of polarity (the polar component of the solubility parameter for PVC was 550 $J^{1/2}\cdot cm^{3/2}\cdot mol^{-1}$ and for PVDC it was 1100 $J^{1/2}\cdot cm^{3/2}\cdot mol^{-1}$).

Table 2.1- Summary of surface roughness results.

Substrate	R_q (nm)	R_a (nm)	D (nm)
Glass	23	11	50
Steel	28	17	-
LDPE	34	22	120
HDPE (s)	36	28	130
PP	51	38	200
HDPE (i)	52	40	410
HDPE (r)	130	91	740

The results from the contact angle experiments determining the contribution of the thermodynamic work of adhesion to cling are presented in Tables 2.2 and 2.3. Contact angle experiments were conducted four times on each material. Table 2.2 shows the data from the contact angle measurements as well as comparative data from the literature[27] for the polar and dispersive components of the surface energy. The surface energy values for the three test liquids are also presented[7]. Although experiments were conducted for each of the film-substrate combinations, the experimentally determined work of adhesion was primarily dependent on the substrate. Therefore, the W_a values are shown in Table 2.3 for each of the substrates; the W_a values for the various films attached to a given substrate are experimentally identical.

The tensile test results for the PVC and PE films show initial elastic regions followed by large plastic regions, with ultimate failure at strains greater than 100 percent as shown in Fig. 2.4. The PVDC films exhibited more brittle behavior, fracturing at less than 20 percent strain. By comparing the stress-strain curves obtained from both machine and transverse directions, residual orientation present in the films from processing was apparent only in the plastic region of stress-strain behavior for the PE film. A summary of the elastic moduli and yield strengths for each of the three films along with an average film thickness are presented in Table 2.4. It is impossible to correlate these data for the PVC and PVDC films with results from the literature due to the unknown plasticizer present within each film. For PE, the literature[29] gives values of the elastic modulus between 102 and 240 MPa and a yield strength equal to 8 MPa. Because of the thickness of the films, it is quite difficult to observe permanent deformation of the films, indicative of plastic behavior. With the results shown in Table 2.4, the non-dimensionalized peel force (Eq. 2-2) was calculated for each of the test systems. The results from this analysis suggest that plastic behavior may be associated with the variable angle peeling of the PVC film from the LDPE substrates.

As was previously discussed, the amount of charge present on the film and substrate was measured after each test. In all cases where intermediate to significant charge transfer occurred, the film retained a negative charge while the substrate had a lower positive charge. Charge transfer involving PE films was always classified as low. Due to the limited sensitivity of the equipment, it was often difficult even to measure a surface charge density in these cases. The PVDC films most often showed intermediate charge transfer and occasional significant charge transfer. The PVC films showed both intermediate and significant charge transfer. There was no correlation between substrate

Table 2.2 - Experimentally determined surface energy values for each material and values taken from the literature for each material and test liquid. The literature values are shown in parenthesis.

	Material	γ (mJ/m^2)	γ^d (mJ/m^2)	γ^p (mJ/m^2)
Substrates	LDPE	38.0 (32.4)	35.1 (31.3)	2.9 (1.1)
	PP	38.9 (31.0)	34.7	4.2
	HDPE-smooth	35.4	35.1	0.3
	HDPE-intermediate	37.8	37.0	0.8
	HDPE-rough	38.8	35.8	3.0
Films	PVC	48.6 (41.5)	42.7 (40.0)	5.9 (1.5)
	PE	49.9 (32.4)	40.8 (31.3)	9.1 (1.1)
	PVDC	48.3 (45.0)	44.5 (42.0)	3.8 (3.0)
Liquids	Water	(72.2)	(22.0)	(50.2)
	Formamide	(58.3)	(32.3)	(26.0)
	Bromo-Napthalene	(44.6)	(44.6)	(0.0)

Table 2.3 - Experimentally determined thermodynamic work of adhesion values for each substrate. These results are valid for each of the three films tested.

Substrate	W_a (mJ/m^2)
LDPE	87
PP	88
HDPE-smooth	80
HDPE-intermediate	84
HDPE-rough	87
glass	180[†]
steel	250[†]

[†] The work of adhesion values for the glass and steel are approximate estimates and an organic layer was assumed to be present after cleaning with methanol[28].

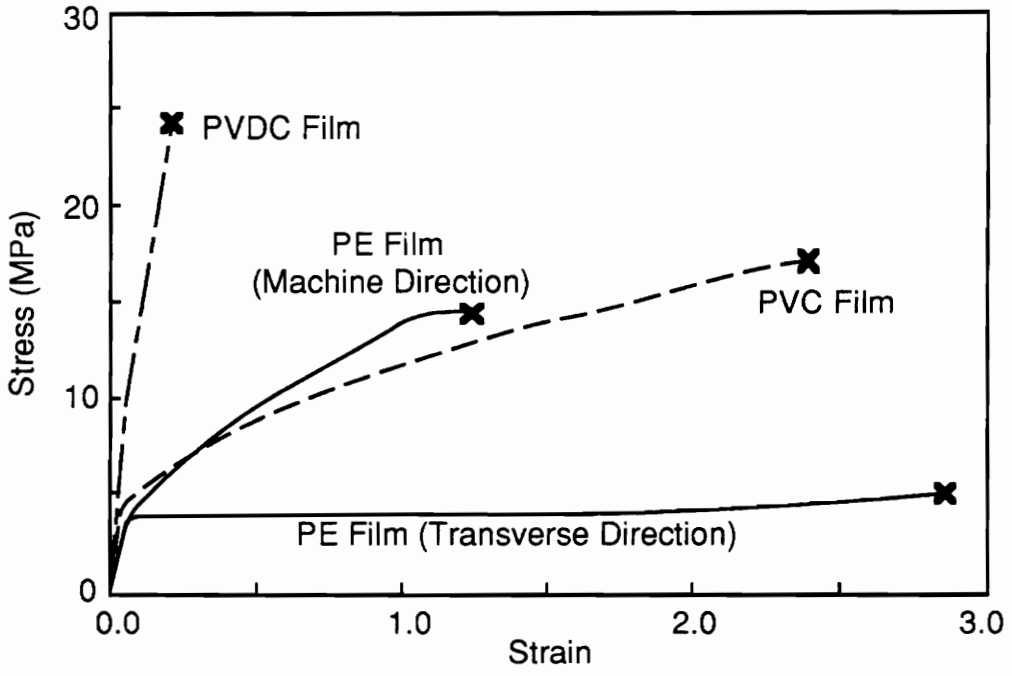

Figure 2.4 - Stress-strain curves of PVC, PE (machine and transverse directions), and PVDC films. There was no distinction in the machine and transverse directions for the PVC and PVDC films.

Table 2.4 - Material properties and thickness of polymeric films.

Films	Elastic Modulus (MPa)	Yield Strength (MPa)	Thickness (μm)
PVC	120	4.6	19
PE	80	3.5	16
PVDC	210	9.0	21

material and charge transfer, other than that the steel substrate displayed very low charge density. This is due to the conductive nature of the material.

The results from the peel tests for the various film-substrate systems shown in Figs. 2.5 and 2.6 are given in terms of the critical strain energy release rate, G_c, with units of mJ/m^2. The error bars shown represent one standard error. The results shown in Fig. 2.5 show the values of G_c for each of the three films on the five substrates determined from the variable angle peel test. The substrates are shown in order of roughness, from smoothest to roughest. (The HDPE substrate used here is the smoothest of the three HDPE substrates.) The effect of varying surface roughness is shown in Fig. 2.6. The values are shown for G_c for the three films debonding from the various roughness surfaces of HDPE during the variable angle peel test. It should also be noted that the charge transfer dropped significantly for the case of the HDPE-rough substrate.

In the variable angle peel tests, it was not possible to control the rate of peel, but a few observations of rate are warranted. For the rough HDPE substrate and for the steel substrate, the films remained attached until the critical angle was reached and debonding progressed very quickly (greater than 50 mm/s). For the other cases, a statistical analysis of peel rate showed no discernible correlation between peel rate and strain energy release rate for any of the cases. For these film-substrate systems, it was typical for peel rates to vary between 1 mm/s and 20 mm/s.

The tests conducted to highlight the effects of long-range electrostatic attractive forces showed no difference in the measured strain energy release rates. Although substrate widths were varied (between 50 and 100 mm) and peel angle was varied (65°, 90°, and 104°) no changes in debonding energy were observed. In conjunction with the observation of the free-hanging end of the film, it is possible to conclude that long-range attractive forces do not play an observable role in the cling of these films to these substrates and that the measured cling is due solely to short-range attractive forces.

Tests were also conducted with PVC film and smooth and rough HDPE substrates by not removing the charge present on the film before contact. For the case of the smooth substrate, there was no observable difference in debonding energy when comparing the results to the case where the charge on the film was neutralized. The film, with its inherent charge, placed on the roughened substrate showed an approximately 50 percent drop in debonding energy when compared to the neutralized film case. This is due to the mixed attractive and repulsive charge present on the film and the decreased opportunity for contact charging resulting from the roughened surface.

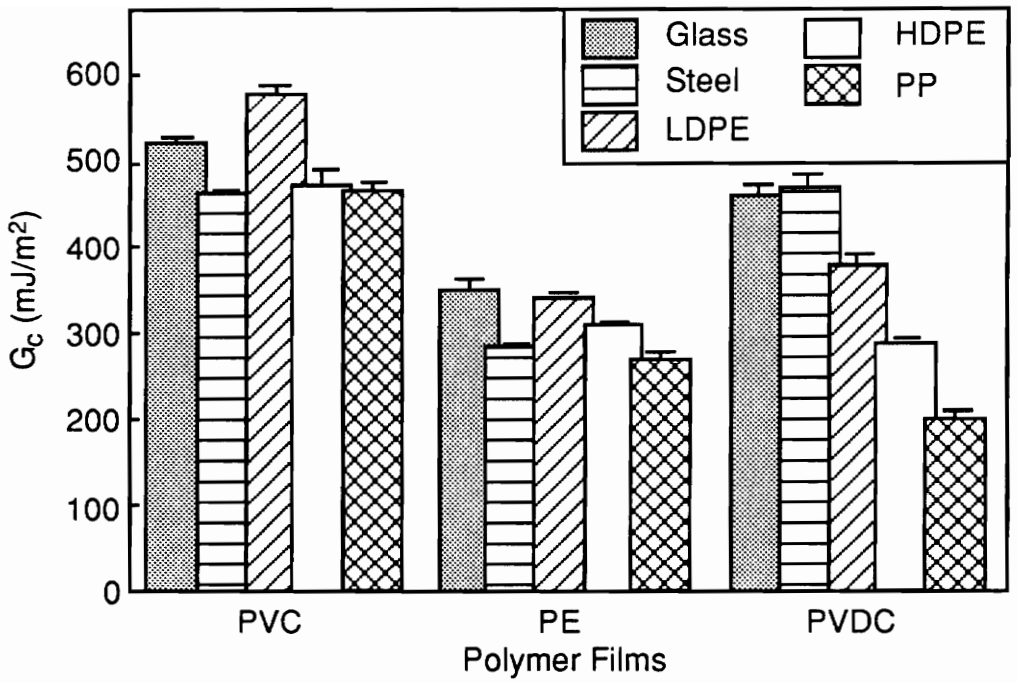

Figure 2.5 - Critical strain energy release rates, G_c, for the various film-substrate combinations.

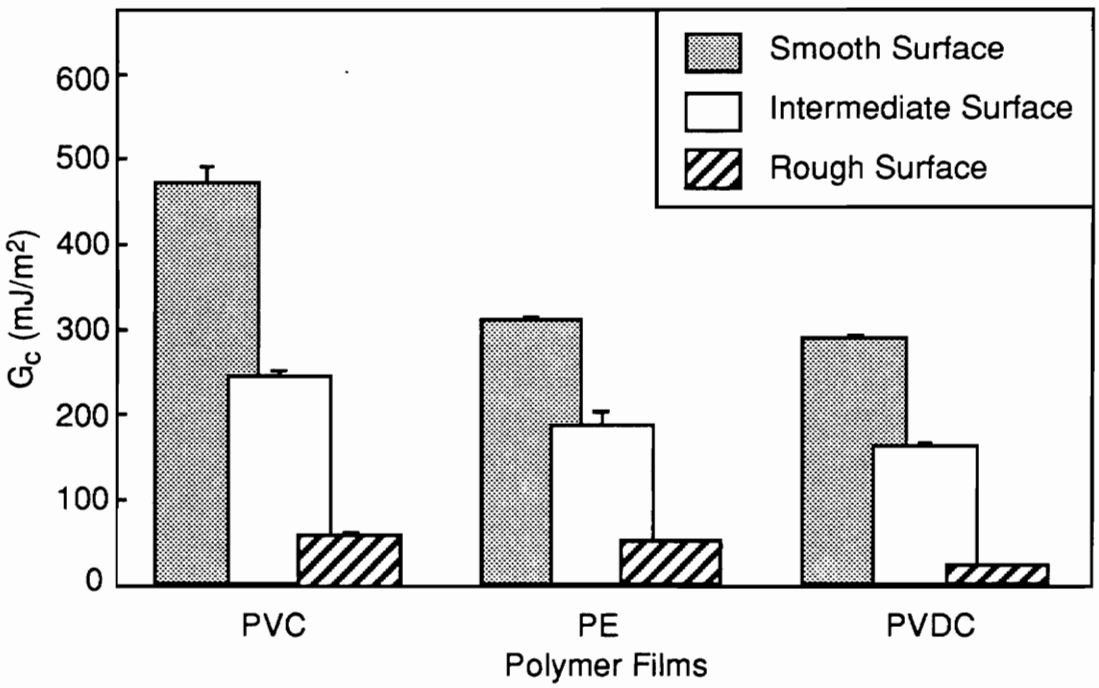

Figure 2.6 - Critical strain energy release rates, G_c, for the various films on the three HDPE surfaces of varying roughness. The error is not noticeable for the PE and PVDC films attached to the rough HDPE substrates.

The results from the 90° peel tests conducted to study rate effects on measured G_c are shown for the three films in Figs. 2.7, 2.8, and 2.9. These results have only been obtained for the three films attached to the HDPE-smooth substrate. The figures show data points of peel rate versus critical strain energy release rate. The error bars represent plus and minus one standard deviation of the experimental results (three to ten tests were conducted for each film and rate combination).

2.4 Discussion

The greatest variation in strain energy release rates caused by changing substrates was due simply to increasing surface roughness. Even though the roughest substrate appears smooth to the naked eye, the impact of minor surface variations cannot be overstated. This is most likely a result of the importance that surface roughness has on multiple mechanisms affecting cling. Although the contact angle measurements demonstrated little change in W_a for increasing roughness from smooth to rough HDPE, the peel tests showed an average decrease in G_c of approximately 90 percent from smooth to rough HDPE substrates. Because of imperfect wetting, reduced contributions from both van der Waals attractive forces and contact electrification are expected.

An exact understanding of the contribution to cling from thermodynamic forces is difficult since surface roughness leads to major discrepancies between the predicted work of adhesion from contact angle studies and the actual debonding energy as measured by peel tests. In fact, the predicted work of adhesion resulting from surface energy studies is greater than the measured total work of adhesion for the various films attached to the rough HDPE substrates. To limit the effect of surface roughness in this conclusion, the studies involving the four smoothest substrates are considered (LDPE, smooth HDPE, glass, and steel). By considering the predicted work of adhesion values, determined from contact angle studies, as maximum limits on the contribution to cling due to van der Waals forces, it is possible to attribute the remaining debonding energy to a combination of electrostatic attraction and plastic and viscoelastic dissipation. Table 2.5 shows the approximate contribution to cling due to these other mechanisms as a percentage of the total debonding energy for the polar films (PVC and PVDC) films, the non-polar film (PE), and the four smoothest substrates.

Since varying the peel angle and the substrate width of a number of tests involving the PVC film-HDPE substrate system had no noticeable effect on debonding energy, long-

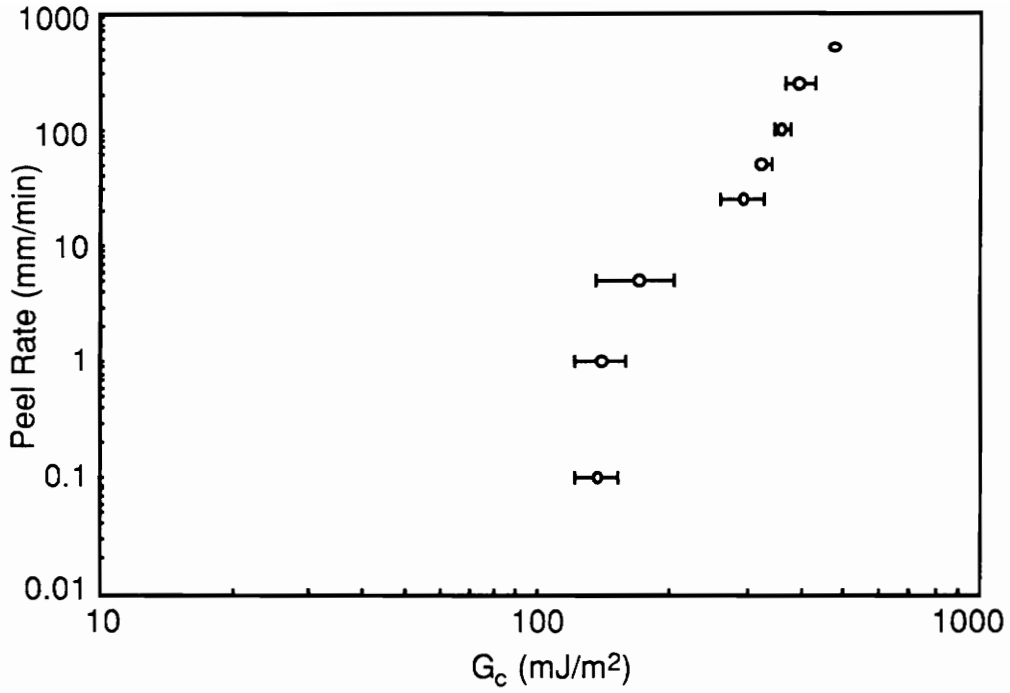

Figure 2.7 - Peel rate versus G_c for PVC film attached to HDPE-smooth substrate.

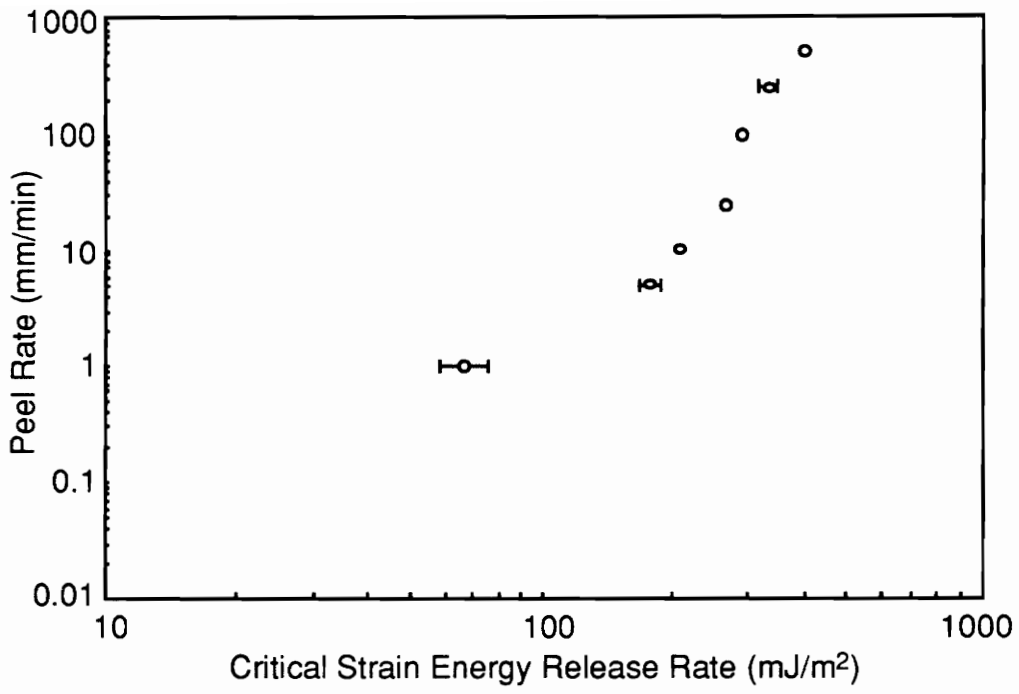

Figure 2.8 - Peel rate versus G_c for PE film attached to HDPE-smooth substrate.

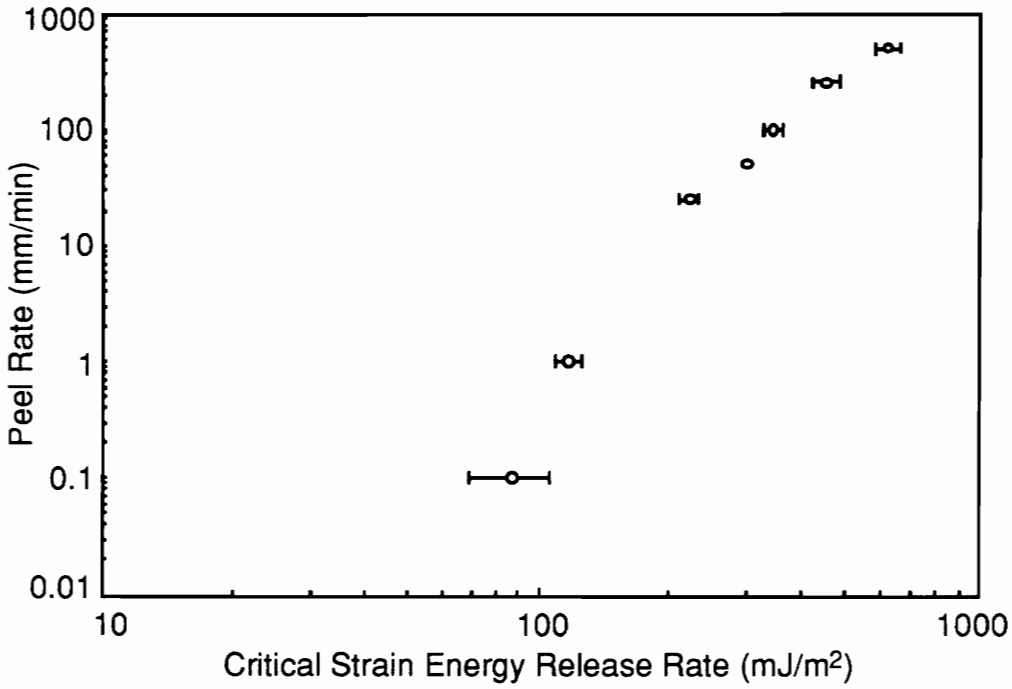

Figure 2.9 - Peel rate versus G_c for PVDC film attached to HDPE-smooth substrate.

Table 2.5 - Approximate percentage of contribution to cling due to a combination of electrostatic attraction and plastic and viscoelastic dissipation.

Substrates	Polar Films (PVC and PVDC)	Non-Polar Film (PE)
Polymer (LDPE, HDPE)	~ 80%	~ 75%
Pyrex Glass	~ 65%	~ 50%
Steel	~ 45%	~ 10%

range attractive forces are believed to have no influence on cling. As was mentioned previously, plastic dissipation may only play a role in debonding the PVC film from the LDPE substrate. Therefore, electrostatic attractive forces acting within the process zone and viscoelastic dissipation do play a significant role in the adhesion process. From Table 2.5, this combined contribution to cling between the various substrates and the polar films (PVC and PVDC) is similar for each of the substrates and higher than the contribution from the non-polar film (PE) for the glass and steel substrates.

It is also interesting to note that, although the PVC and PVDC films show relatively similar contributions to cling due to electrostatic attraction, the PVC and PE films exhibit similar patterns of behavior when comparing the experimentally determined strain energy release rates. The values of G_c for the PVC and PE films for each of the various substrates are all within 100 mJ/m^2 of one another. The G_c values for the PVDC film range approximately between 200 - 500 mJ/m^2.

In addition to information from Ref. 14, all of the films caused sparking when the film was applied to glass substrates. Electrical breakdown was also evident by hearing static from an AM radio during peeling of the polar films (PVC and PVDC). Therefore, although each of the polymers has the potential to carry significant charge , it is possible that the approximately 50 percent higher values of G_c associated with PVC, when compared with PE, may be attributed to increased charge transfer during contact, increased charge retention during peel, and/or the highly polar nature of PVC.

The three films also show rate dependency for measured G_c. As is shown in Figs. 2.7 - 2.9, higher peel rates are associated with higher values of G_c, which is typical for many bonded systems. Since the data are shown on log-log scales, the magnitude of the range of debond rate and G_c is quite large, suggesting that time dependency may play a major role. Possible sources of time dependency include the viscoelastic behavior of the film and the potential for time dependent electrostatic discharge. Additional work must be done before suggesting more definite conclusions about the source of time dependent effects, whether viscoelastic or electrostatic, on the system.

3.0 AN ANALYSIS OF THE EFFECTS OF VISCOELASTICITY ON ADHESIVE SYSTEMS INVOLVING CURVATURE MISMATCH

Stresses may arise within an adhesive bond due to a mismatch of curvature between the stress-free shape and the final bonded shape of two adherends. Curvature mismatch may occur in many industrial applications, due to design or as a result of environmentally induced curvature within the adherend. Curvature mismatch may also be used as an experimental device as a means for characterizing different adhesives. In either case, it is beneficial to have an accurate understanding of the mechanics of the curvature mismatch system. This work focuses on understanding the mechanics of this type of problem, creating models to predict bond behavior for systems subjected to such curvature mismatch, and testing such systems within the laboratory. This work is an extension of earlier work[27,31], with the addition of time dependency included in the adhesive model and with the addition of experimental investigations.

Examples of curvature mismatch systems are shown in Fig. 3.1. In each of these cases, a flexible adherend is shown above a rigid substrate. (The analysis presented in this work may also be used for the bonding of two flexible adherends with different curvatures.) Any analytical technique modeling these bonded systems must account for the material properties of the adherend(s), the material properties of the adhesive, and the geometry of the system. The geometry of the debond tests conducted for this work is shown in Fig. 3.2. For these tests, an initially flat steel adherend is bonded to a circular, rigid glass substrate with a double-sided pressure sensitive adhesive. Since this is the experimental system which will be studied, this geometry will be considered in all subsequent derivations.

To obtain an accurate and meaningful model of an adhesive bond, it is necessary to have an accurate model of the adhesive itself. Section 3.1 of this chapter describes both the theoretical and experimental analyses required to model the adhesive. Two different models will be used, the Maxwell fluid (a viscoelastic element) and the Bingham element (an elastic-viscoplastic element).

Section 3.2 presents the basics of the derivation of the beam on an elastic foundation solution. This work is necessary to provide a foundation for the derivations of two analytical techniques presented in Sections 3.3 and 3.4 which attempt to model bond behavior and predict debond rates. In Section 3.3, the Maxwell fluid is used to model the

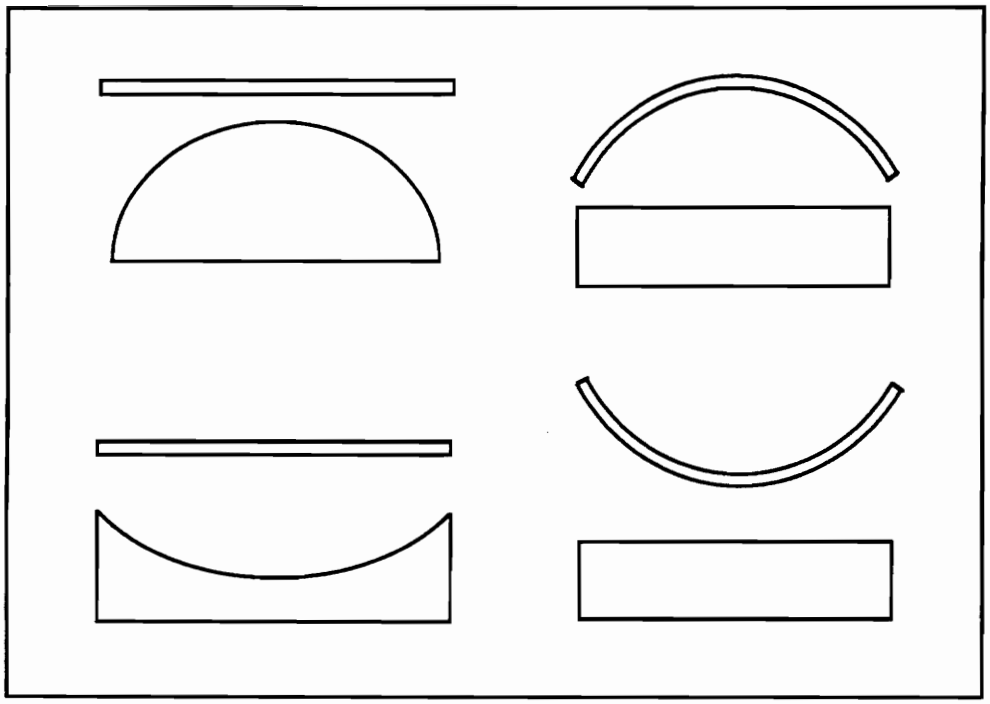

Figure 3.1 - Sample cases showing the curvature mismatch between a flexible adherend and a rigid substrate.

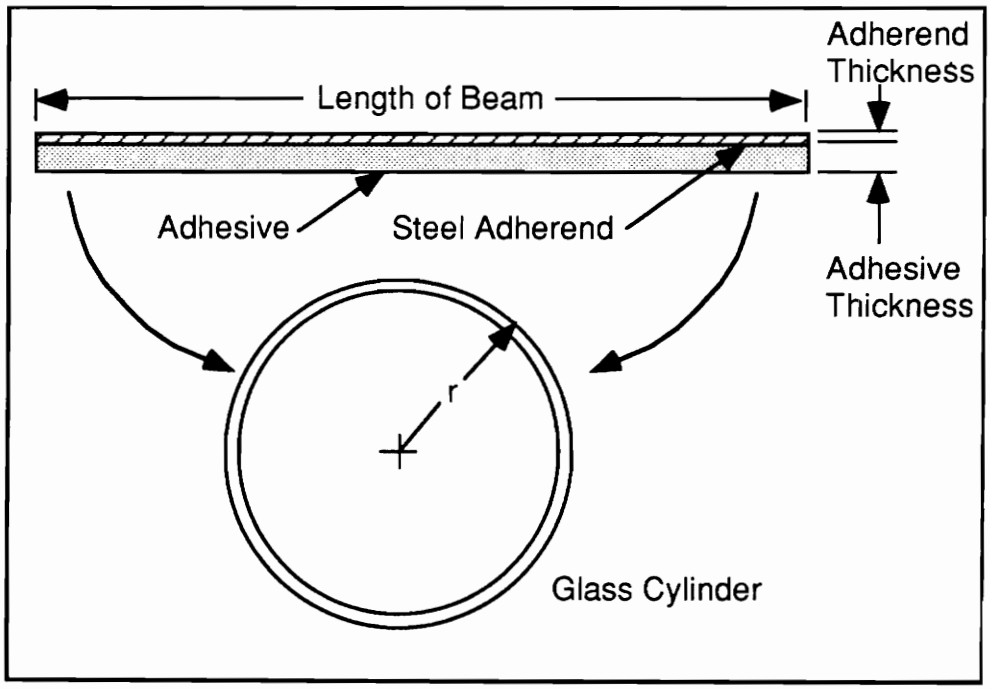

Figure 3.2 - Geometry of the debond tests.

adhesive layer, thereby introducing time dependency into the solution of the beam problem. In Section 3.4, the beam on elastic foundation solution is used with the Bingham element to model the adhesive. Both analytical techniques use recursive solutions to predict debonding of the adherend over time. Section 3.5 introduces the experimental system in greater detail while Section 3.6 presents the results of the experiments. These results are discussed in Section 3.7. It is hoped that this work will increase the current understanding of this phenomena and may lead to improved testing procedures for a variety of adhesive systems.

3.1 Adhesive Models

An accurate adhesive model is necessary when using any analytical technique which models the behavior of an adhesively bonded system. In this work, a pressure sensitive adhesive used in debond experiments is modeled in two different ways: using the Maxwell model (a viscoelastic element) and using the Bingham model (an elastic-viscoplastic element). These two elements are used in two different models to predict and understand adhesive bond behavior. A schematic of the pressure sensitive adhesive, showing a foam core with two layers of adhesive bonding a steel adherend to a glass substrate is shown in Fig. 3.3 (a).

In this section, after introducing the models, the governing differential equations of the models are presented. The equation for the relaxation modulus of the Maxwell model is also shown, since this relation is necessary to characterize the adhesive from the results of the extension tests. The experiments used to characterize the adhesive are then described along with results which are used in determining the constants associated with each adhesive model. Finally, the methods used to obtain those adhesive model constants and the results showing the behavior of each model are presented.

3.1.1 Maxwell Model

The first adhesive element model considered is the Maxwell fluid, shown in Fig. 3.3 (b). This element consists of a linear spring and a linear dashpot in series. Both the spring and the dashpot are subjected to the same stress. The total strain of the element is simply the sum of the strains associated with both the instantaneous response of the

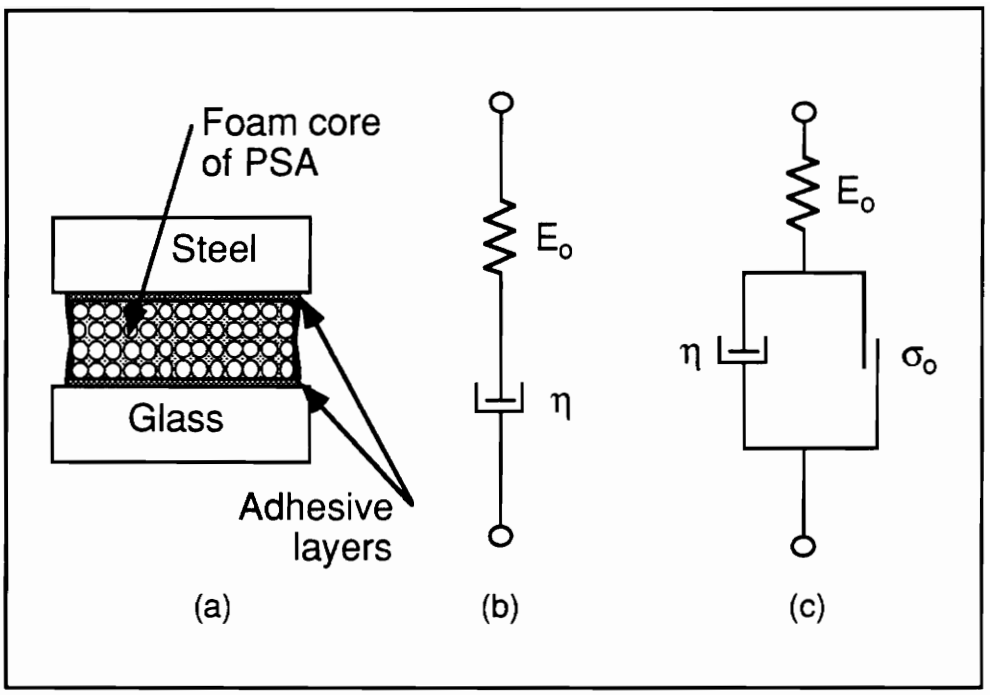

Figure 3.3 - Schematics of the pressure sensitive adhesive (a), Maxwell element (b) and Bingham element (c) which are used to represent the pressure sensitive adhesive.

element, the spring, and the time dependent response of the element, the dashpot. The Maxwell fluid is a linear viscoelastic element, whose governing differential equation is given in the following form:

$$\sigma + \frac{\eta}{E_o}\dot{\sigma} = \eta\dot{\varepsilon} \tag{3-1}$$

- σ is the stress applied to the element
- ε is the total strain associated with the element
- E_o is the spring constant
- η is the dashpot constant

The dot over the stress and strain indicates a derivative with respect to time.

The relaxation modulus of this material, E(t), is given by[32]

$$E(t) = E_o e^{-\frac{E_o}{\eta}t}. \tag{3-2}$$

This definition will be used in Section 3.1.4 to incorporate the experimental results obtained from constant strain rate extension tests into the Maxwell element used to model adhesive behavior.

3.1.2 Bingham Model

The Bingham element is used to model the adhesive in Section 3.4. This elastic-viscoplastic element is shown in Fig. 3.3 (c). It consists of a Hookean spring, of spring constant E_o, in series with a sub-element consisting of a dashpot and slider in parallel. The Newtonian dashpot is represented by a constant η, while a value of yield strength, σ_o, is associated with the slider. For any applied stress less than σ_o, the Bingham element behaves as a linear spring. For stresses greater than σ_o, the slider is free to move, allowing the dashpot to extend over time.

There are two different equations which relate stress to strain for the Bingham element[33], depending on the applied stress. For an applied stress less than σ_o,

$$\sigma(\varepsilon) = E\varepsilon \tag{3-3}$$

while for an applied stress greater than σ_o,

$$\sigma(\varepsilon) = \sigma_o + \eta\dot{\varepsilon}\left[1 - e^{-\frac{E_o}{\eta\dot{\varepsilon}}(\varepsilon-\varepsilon_o)}\right], \tag{3-4}$$

where ε_o is defined as the strain at the elastic limit, $\sigma = \sigma_o$.

3.1.3 Experimental

Experiments were conducted using an Instron universal test frame. The tests were used to characterize the adhesive which bonds the steel adherends to the glass cylinders in the debond experiments. The Maxwell and Bingham models were used to fit the data obtained from the results of the tensile tests. Although different information was used to obtain the constants of the two models, only one set of tests were performed. The adhesive tested was the 3M Scotch-Mount brand Y-4248 neoprene foam tape. It is a pressure sensitive adhesive consisting of a foam liner with an acrylic adhesive on both sides. Additional information about the adhesive is presented in Section 3.5.

Each adhesive test specimen was cut from the roll of the pressure sensitive adhesive to obtain a disk of diameter 6.20 mm and thickness 1.14 mm. Two flat substrates, one of glass and one of steel, were attached to the testing machine, cleaned with acetone, and bonded together with the pressure sensitive adhesive disk. The substrates were chosen to represent the actual materials to be tested in the debond experiments.

Before testing began, the substrates bonded with the adhesive were compressed to approximately -50 kPa and held for 15 minutes. Three tests were then conducted at the four following strain rates: $1.6(10^{-4})$ s^{-1}, $1.6(10^{-3})$ s^{-1}, $1.6(10^{-2})$ s^{-1}, and $1.5(10^{-1})$ s^{-1} (these are associated with rates of 0.011 mm/min, 0.11 mm/min, 1.1 mm/min, and 10 mm/min).

The resulting data was expressed first in Fig. 3.4, where one typical curve of stress versus strain is shown for each of the four strain rates. These data were used to determine the constants associated with the Bingham model in Section 3.1.4. In addition to obtaining stress versus strain data, the strain at failure was assumed to be independent of strain rate for the strain rates that were tested. The experimental results suggested no dependency on strain rate for the rates tested; it is unknown whether this is a valid assumption for much lower rates. The average ultimate strain, ε_u, was found to be 0.835. This value corresponds to a maximum extension of 0.951 mm.

The stress strain data are also shown in Fig. 3.5 as stress versus time for the four rates tested. The same sample curves as shown in Fig. 3.4 are shown here. In this case, the horizontal axis from Fig. 3.4 is simply divided by the associated strain rates of the four tests in order to show the stress at a given time. These data were used in obtaining the

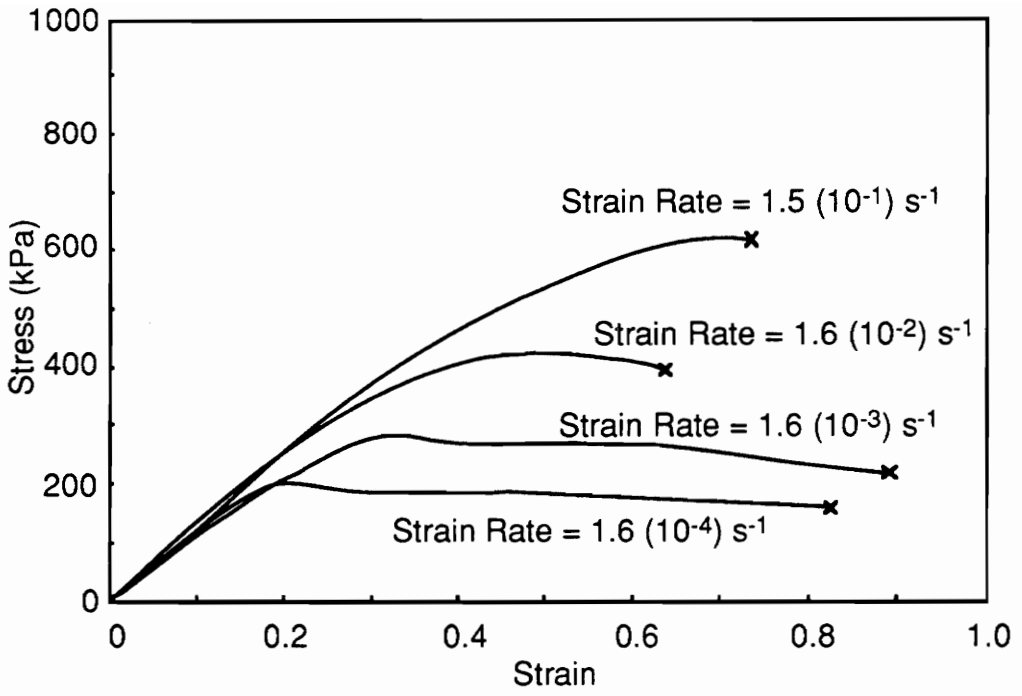

Figure 3.4 - Typical experimental results of stress versus strain at four different rates.

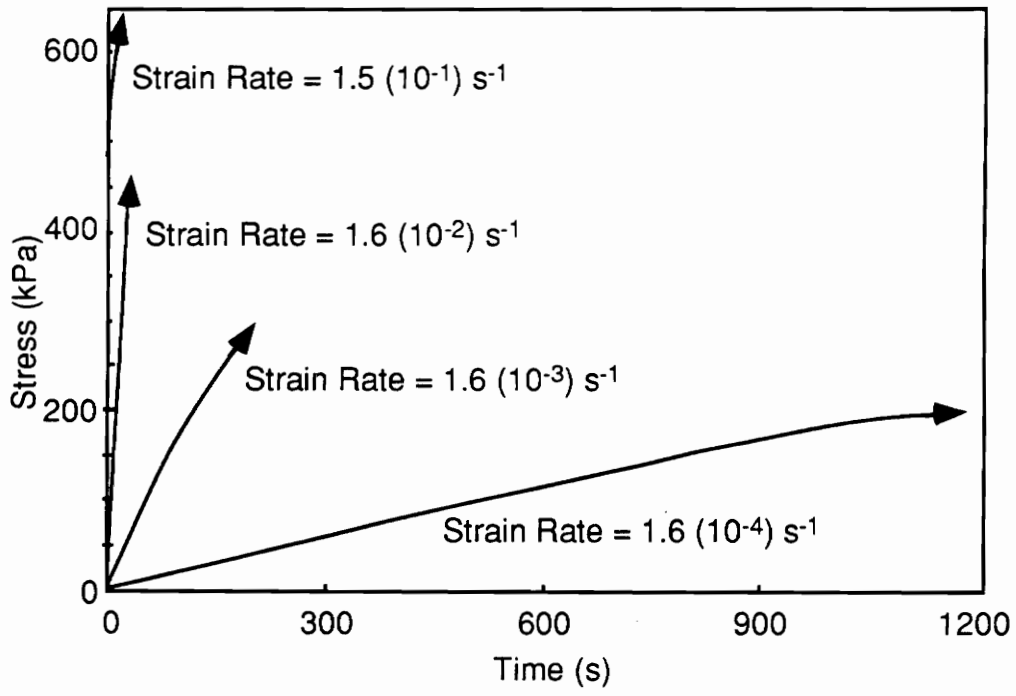

Figure 3.5 - Typical experimental results of stress versus time at four different rates.

constants of the Maxwell model by showing the experimental data in terms of a relaxation modulus as a function of time. Since the Maxwell element assumes linear behavior of the adhesive, only the linear behavior of the adhesive observed from experimentation is considered. The endpoints of the curves shown in Fig. 3.5 do not correspond to failure.

3.1.4 Modeling the Adhesive

The results of the experimental analyses are used to determine the constants which characterize the two adhesive models. The Maxwell model requires values for E_o and η, while the Bingham model requires values for E_o, η, and σ_o. For both cases, the analytical curves were fit to the experimentally obtained curves of relaxation modulus versus time (for the Maxwell model) and stress versus strain (for the Bingham model). Since relaxation experiments were not conducted, the relaxation modulus was determined analytically. Modeling the adhesives in these ways implies that certain assumptions must be made for each case. These assumptions must also be considered in latter sections, when comparing the experimental results of the debond tests to the predicted results utilizing these two models.

3.1.4.1 Maxwell Model

The plot of relaxation modulus, E(t), versus time is used to apply the results from the experiments conducted to characterize the adhesive. Since it is assumed that the material is linear, it is possible to make use of Boltzmann superposition to obtain strain as a function of multiple loads. This assumption allows for the writing of the relationship between stress and strain for a constant strain rate in terms of a hereditary integral in the following form:

$$\sigma(t) = \int_0^t E(t-\tau)\frac{d\varepsilon}{d\tau}d\tau. \qquad (3\text{-}5)$$

By taking the derivative with respect to time of both sides and by considering that the derivative of strain, ε, with respect to time is the strain rate, $\dot{\varepsilon}$, it is possible to write the following equation for the relaxation modulus:

$$E(t) = \frac{1}{\dot{\varepsilon}}\frac{d\sigma}{dt}. \qquad (3\text{-}6)$$

With Eq. 3-6, it is possible to take the data shown in Fig. 3.5 and plot it in Fig. 3.6 as relaxation modulus versus time. The same four curves from the previous figures have

again been used. The values of relaxation modulus of the adhesive at the two higher strain rates are shown as points, since after a very short time this material ceases to behave linearly.

To make use of the Maxwell model, it is necessary to determine two variables: E_o and η. In theory, all of the curves shown plotted in Fig. 3.6 should fall along the same curve, which would then be used to characterize the adhesive in terms of E_o and η. From Eq. 3-2, it is apparent that the value of E_o can be determined from the intercept with the vertical axis (at t = 0). From the tests that were conducted, this was found to be approximately equal to 1,220 kPa. To obtain the value for η, it was simply necessary to fit the curve in the best manner to the experimental curves. A value of η equal to 30 MPa-s was chosen.

These experimentally determined values are applied to the Maxwell model so that the relaxation modulus may be plotted as a function of time. This result is shown in Fig. 3.6 as a dashed curve. It is important to consider that this curve is obtained experimentally, and so possesses any error from the experimental results. In addition, this model, valid only in the linear region of the material's response to loading, considers the entire response of the material to a given loading as linear until failure. The significance of this assumption will be addressed Section 3.7.

3.1.4.2 Bingham Model

The results plotted in Fig. 3.4 were used to determine the three constants associated with the Bingham model: E_o, η, and σ_o. The same spring constant (E_o) obtained in Section 3.1.4.1 was also used to model the linear elastic behavior of the adhesive. The stress-strain curves obtained from the lowest strain rate experiments represent the behavior of the adhesive subjected to an infinitesimal strain rate. From this assumption, the yield strength of the model, σ_o, has a value of 170 kPa.

Finally, it was necessary to determine the value of the dashpot constant. This was accomplished by fitting the analytical curves obtained from the model to the experimental curves. Since the debond tests that were conducted involved low strain rates, the experimental curves associated with the low strain rates were given greater importance when the adhesive model was generated. Therefore, the dashpot constant was taken to have a value of 57.6 MPa-s. As previously discussed, the ultimate strain was assumed to be 0.835.

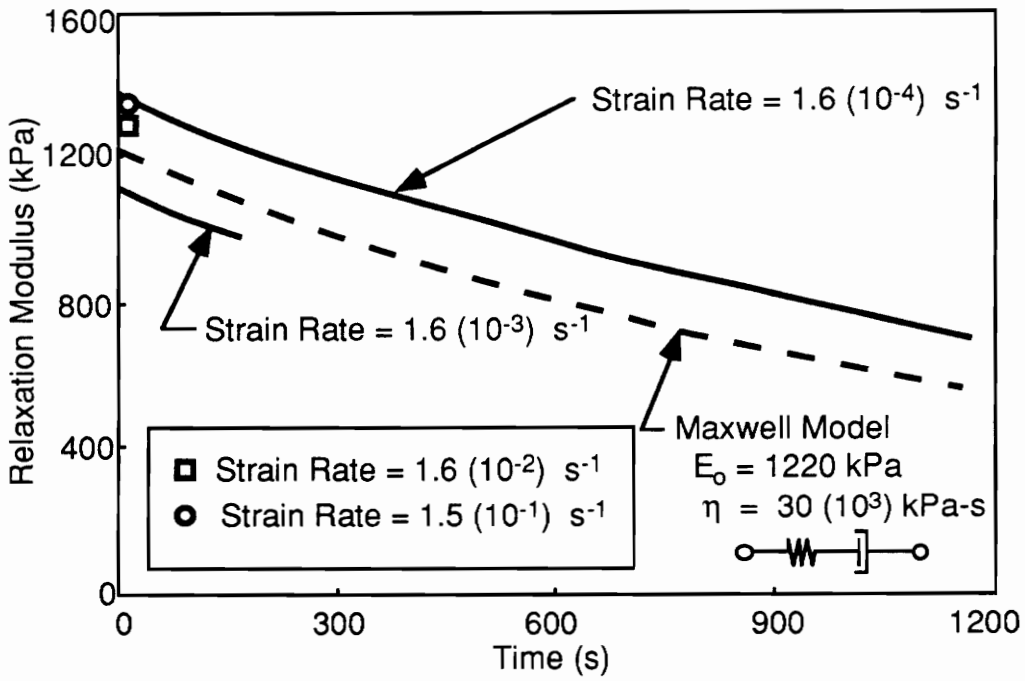

Figure 3.6 - Typical experimental and Maxwell model results of relaxation modulus versus time.

These constants, when applied to the Bingham element, produce results which are plotted in Fig. 3.7. The experimental results from Fig. 3.4 are also shown as dashed curves. The model is seen to behave more realistically for the lower two strain rates which were tested. For the higher rates, the model fails to predict the actual behavior of the adhesive when compared to the experimentally determined results. The ultimate strain is shown independent of strain rate, according to the assumption.

By choosing the value of σ_o to be 170 kPa, this model suggests that for any applied stresses less than 170 kPa, no flow will occur over any length of time. This phenomenon provides a lower bound to the projected debond rate determined from any solution incorporating this model if failure is assumed to occur only when strain exceeds a critical value. Therefore, if the stress is less than 170 kPa within an adhesive bond, this model predicts no debonding of the adherend.

3.2 Beam on Elastic Foundation Analysis

To provide a foundation to the work described in the remainder of this chapter, in particular Sections 3.3 and 3.4, a review of the fundamentals of the derivation of the beam on elastic foundation solution for bonded systems involving curvature mismatch is presented. In addition, a sample of the type of results obtained from a beam on elastic foundation analysis is included. A more detailed description of the derivation as well as analytical results obtained from the solution may be found in other work[30,31].

3.2.1 Derivation of the Beam on Elastic Foundation Solution

The response to a loading due to the curvature mismatch between a flexible, elastic adherend and a rigid substrate is analyzed using a beam on elastic foundation model, or Winkler foundation. From fundamental mechanics, the relationship between deflection of a beam and the associated distributed force due to the stiffness of the foundation yields the following fourth-order differential equation[34,35].

$$EI\frac{d^4u(x)}{dx^4} = -ku(x) \tag{3-7}$$

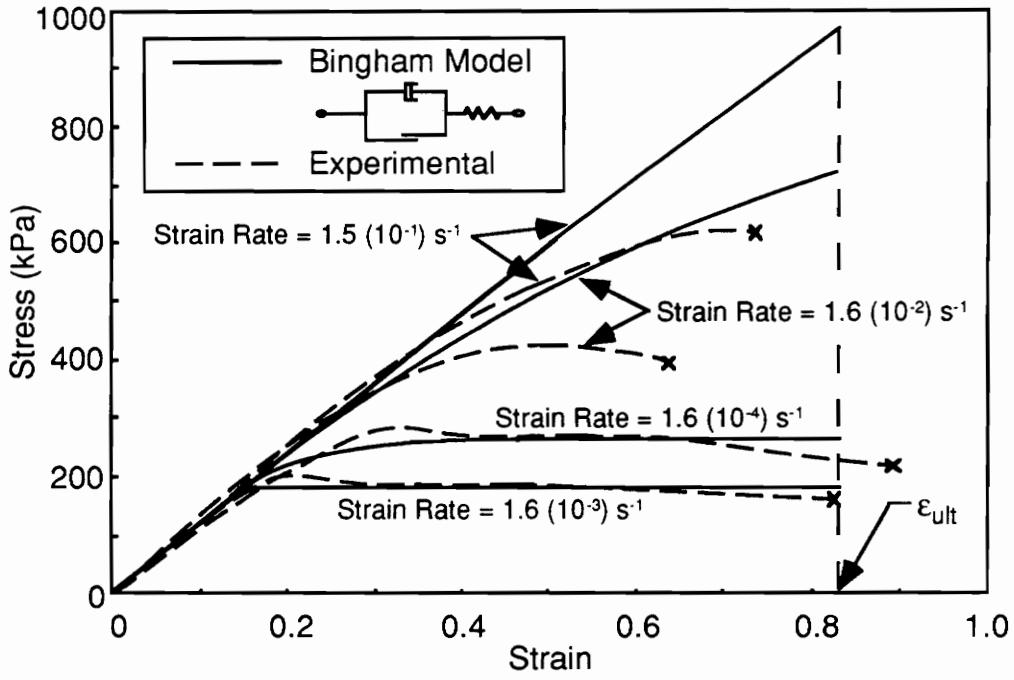

Figure 3.7 - Bingham model and experimental stress versus strain curves of the adhesive at various strain rates.

- EI is the bending stiffness of the beam
- u is the vertical deflection of the beam
- x is the position along the beam length
- k is the foundation stiffness

For this equation to be valid, it is assumed that the foundation resists transmitted loads in a linear elastic manner and that the displacements of the beam are small.

Since the adhesive is considered linear elastic, it is possible to define the foundation stiffness from Eq. 3-7 in terms of the elastic modulus, thickness, and width of the adhesive layer as follows:

$$k = \left(\frac{w}{h}\right) E_a \tag{3-8}$$

- E_a is the elastic modulus of the adhesive
- w is the width of the adhesive
- h is the thickness of the adhesive

After inserting the definition of the foundation stiffness from Eq. 3-8 into Eq. 3-7, the differential equation is simplified by utilizing the variable λ, which is defined as follows:

$$\lambda = \left(\frac{E_a w}{4EIh}\right)^{1/4}. \tag{3-9}$$

Equation 3-7 is rewritten in the following form:

$$\frac{d^4u(x)}{dx^4} + 4\lambda^4 u(x) = 0. \tag{3-10}$$

Four boundary conditions are then necessary to solve for the beam deflection. From the physics of the problem, it is evident that there is neither a moment nor a shear force applied at either end of the beam. Since there are no externally applied loads, the beam deflection must be due solely to the difference in curvature between the stress-free shape of the beam and the shape of the substrate it is attached to. The stress-free shape of the beam is given by[30]

$$u_o(x) = \frac{x^2}{2\rho}. \tag{3-11}$$

The initial curvature is assumed to be constant and adequately modeled by Eq. 3-11 over any small region. The boundary conditions at both ends, -L and +L, may be written as follows:

$$M(\pm L) = EI \left.\frac{d^2(u - u_o)}{dx^2}\right|_{x=\pm L} = 0 \text{ and} \tag{3-12}$$

$$V(\pm L) = EI \left.\frac{d^3(u - u_o)}{dx^3}\right|_{x=\pm L} = 0. \tag{3-13}$$

The radius of curvature, ρ, is measured to the neutral axis of the adherend. It represents the difference in curvature between either an initially curved beam bonded to a flat substrate or between an initially flat beam bonded to an initially curved substrate.

From Eqs. 3-12 and 3-13, it is apparent that the boundary conditions for the deflection, u(x), at the endpoints of the beam may be written as:

$$\left.\frac{d^2u}{dx^2}\right|_{x=\pm L} = \frac{1}{\rho} \text{ and } \left.\frac{d^3u}{dx^3}\right|_{x=\pm L} = 0. \tag{3-14}$$

This is equivalent to the problem of an initially flat beam attached to a flat substrate with a constant moment applied at both ends.

The solution to the homogeneous, fourth-order ordinary differential equation with inhomogeneous boundary conditions is found to be

$$u(x) = \frac{U(x) + U(-x)}{2\lambda^2\rho\left[1 - e^{4L\lambda} - 2e^{2L\lambda}\sin(2L\lambda)\right]} \tag{3-15}$$

where U(x) is defined as

$$U(x) = e^{(L+x)\lambda}\left\{-e^{2L\lambda}\cos\left[(L-x)\lambda\right] + \cos\left[(L+x)\lambda\right] + e^{2L\lambda}\sin\left[(L-x)\lambda\right] + \sin\left[(L+x)\lambda\right]\right\}.$$

This solution will be referred to in Section 3.3 as the initial condition for the beam on a viscoelastic foundation problem. In Section 3.4, the solution of the beam on elastic foundation problem is again used to obtain the stress distribution applied to a series of Bingham elements. Since the adhesive is still considered to act in a linear elastic manner, Hooke's law is used to write the following relation (considering that strain is simply the deflection divided by the adhesive thickness):

$$\sigma(x) = \frac{E_a u(x)}{h}. \tag{3-16}$$

As is expected, the stress is linearly proportional to the deflection of the beam.

3.2.2 Sample Results

Although Section 3.2 is intended as a review before considering additional solutions, sample results are presented for one physical system to provide some insight into the physics of the elastic problem. The system analyzed is similar to that shown in Fig. 3.2. For this case, the following material properties and geometries were used:

- E = 210 GPa (modulus of steel adherend)
- t = 0.254 mm (thickness of adherend)
- E_a = 1.22 MPa (modulus of the adhesive)
- h = 1.14 mm (thickness of the adhesive)
- w = 12.7 mm (width of adherend and adhesive)
- ρ = 35 mm (radius of the difference in curvature between the adherend and the substrate)

The results given in Fig. 3.8 show two types of information. The solid curves represent the deflection of four beams of differing half-lengths (10 mm, 20 mm, 30 mm, and 40 mm). (Due to the symmetry of the problem, only one-half of the total beam length is shown. The deflection curves are symmetric about the vertical axis. This format is used in the remainder of this work.) The deflected shapes are similar, in that the free ends have a positive deflection (towards the right-hand side) in addition to a section with negative deflection (moving inward, towards the center of the beam). Since stress is linearly proportional to deflection (Eq. 3-16), these deflections correspond to tensile stresses at the bond tip followed by a region of compressive stress within the bond.

The deflections of bonds of lengths grater than 15 mm have similar shapes. The regions of tensile and compressive stresses are of relatively similar sizes for long beams. As the beam is shortened, the shape of the stress distribution changes.

In addition, the dashed curve in Fig. 3.8 represents the deflection at the endpoint of a beam for the associated beam length. As can be seen, for beams of length greater than 15 mm, this value is constant.

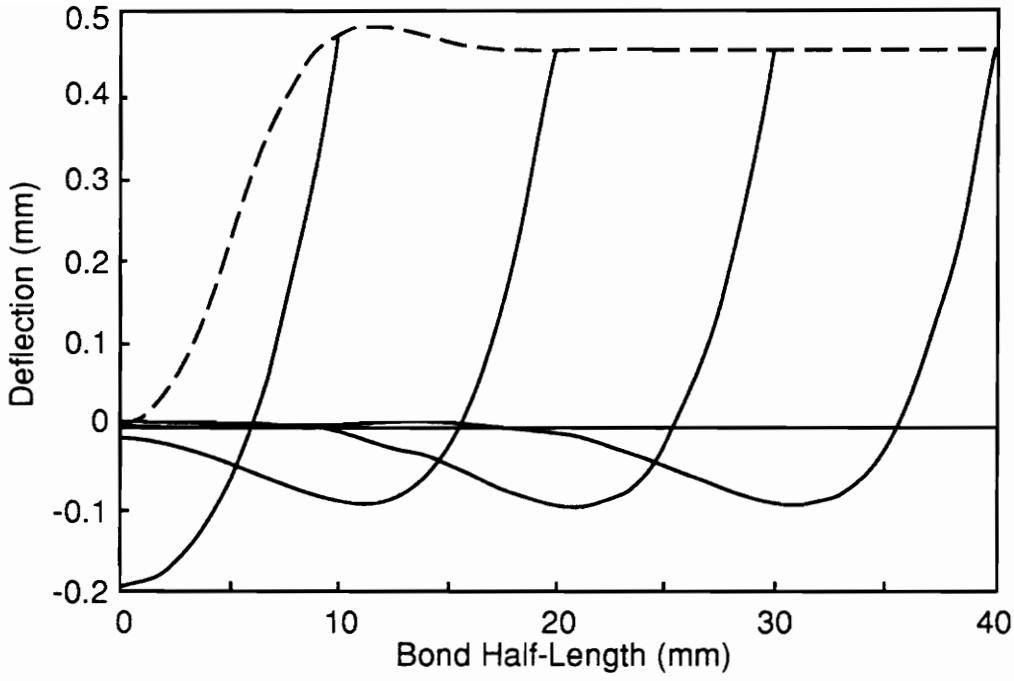

Figure 3.8 - Solution for beam deflection from beam on elastic foundation analysis.

The specific values of deflection for a given beam length are dependent on the material properties and the system geometry. The conclusions discussed here are valid for any situation, since the results presented here may simply be scaled by factors dependent on the material properties and the bond geometry.

3.3 The Beam on a Viscoelastic Foundation

In this section, the response to curvature mismatch between an adherend and an adhesive is modeled by representing the adherend as a linear elastic beam supported by a viscoelastic foundation. Kobayashi and Sonoda[36] presented a similar type of solution obtained for a Timeshenko beam while Kuczma and Switka[37] used the finite element method to solve for the effects of external loading on an elastic beam supported by a viscoelastic foundation. In this work, a closed form solution is presented which requires numerical computations to solve for the beam deflection.

For the following derivation, a Maxwell element is used to represent the viscoelastic response of the adhesive to loadings which result solely from curvature mismatch between an adherend and a substrate. After the solution is obtained, both a uniqueness study and convergence conditions are presented. From the solution to the beam deflection problem, a recursive technique is introduced to model the actual debonding of the adherend from the adhesive. Finally, sample results are presented based both on the solution to the beam deflection problem and on the recursive solution to the debond problem.

3.3.1 Derivation of the Solution

Since there are no applied external loads, the general partial differential equation of an elastic beam on a Maxwell-type viscoelastic foundation is given by[32]

$$EI\left[\frac{\eta}{E_o}\frac{\partial}{\partial t}\frac{\partial^4 u(x,t)}{\partial x^4}+\frac{\partial^4 u(x,t)}{\partial x^4}\right]+\eta\left(\frac{w}{h}\right)\frac{\partial u(x,t)}{\partial t}=0 \qquad (3\text{-}17)$$

- EI is the bending stiffness of the beam
- E_o is the spring constant associated with the Maxwell element
- η is the dashpot constant associated with the Maxwell element
- u(x,t) is the deflection of the beam as a function of position along the beam (x) and time (t)

- w is the width of the adhesive and adherend
- h is the thickness of the adhesive

This equation, of a similar form to Eq. 3-7 for the case of a beam on an elastic foundation, is rewritten in the following form for the remainder of the derivation

$$u_{xxxx,t} + \alpha u_{xxxx} + \beta u_t = 0 \tag{3-18}$$

where

$$\alpha = \frac{E_a}{\eta} \text{ and } \beta = \left(\frac{w}{h}\right)\frac{E_a}{EI}.$$

The subscripts refer to derivatives, i.e. subscript x refers to a derivative with respect to position along the bond length and subscript t refers to a derivative with respect to time.

As was shown in Section 3.2, the boundary conditions for this system also require that both the moment and shear forces at both ends of the beam are zero. Due to the mismatch in curvature, this produces the following conditions

$$u_{xx}(-L) = u_{xx}(L) = \frac{1}{\rho} \text{ and } u_{xxx}(-L) = u_{xxx}(L) = 0 \tag{3-19}$$

where the beam is considered to be of length 2L and the radius of the difference in curvature is ρ.

The initial condition for this problem (at t = 0) is given by the solution to the linear elastic beam on a linear elastic foundation given by Eq. 3-15, and is of the form

$$u(x,0) = g(x). \tag{3-20}$$

The linear elastic solution is used since, at time zero, the Maxwell element may be treated as a single Hookean spring.

The general solution to the inhomogeneous partial differential equation is obtained by using both a separation of variables and a transformation of variables approach. It is necessary to use separation of variables to recast the partial differential equation into two ordinary differential equations and it is necessary to use transformation of variables to remove the inhomogeneity from the boundary conditions. These techniques lead to a solution for u(x,t) of the form

$$u(x,t) = X(x)T(t) + \frac{x^2}{2\rho}. \tag{3-21}$$

By inserting this solution for u(x,t) into the partial differential equation and by regrouping the terms dependent on either the variable time, t, or position, x, the partial differential equation is rewritten as two ordinary differential equations,

$$T_t(t) + \nu T(t) = 0 \tag{3-22}$$

and

$$X_{xxxx}(x) - \left(\frac{\nu\beta}{\alpha - \nu}\right)X(x) = 0 \tag{3-23}$$

where ν is the separation constant. By substituting this solution into the boundary and initial conditions, it is found that

$$X_{xx}(-L) = X_{xx}(L) = X_{xxx}(-L) = X_{xxx}(L) = 0 \tag{3-24}$$

and

$$X(x)T(0) = g(x) - \frac{x^2}{2\rho}. \tag{3-25}$$

The boundary conditions are now homogeneous for the new variable, X, which is dependent only on position, x. It is also interesting to note that the factor added to Eq. 3-21 to remove the inhomogeneity is equivalent to the stress-free shape of the beam given by Eq. 3-11.

The form of Eq. 3-22 suggests that T(t) is proportional to $\exp(-\nu t)$. The arbitrary constants of proportionality will be included in the constants associated with the solution to the second ordinary differential equation, Eq. 3-23.

From Eq. 3-23, it is also apparent that two different forms of the general solution to the ordinary differential equation for the variable X(x) may be used, depending on whether α is greater than or less than ν. If α is less than ν, it has been found that the only solution that satisfies the boundary conditions is the trivial solution. The trivial solution is identical for both cases, i.e. α greater than ν and α less than ν. Therefore, the derivation proceeds for the case $\alpha > \nu$.

In order to simplify the form of Eq. 3-23, the following substitution is made

$$\mu^4 = \frac{\nu\beta}{\alpha - \nu} \tag{3-26}$$

so that Eq. 3-23 is rewritten as

$$X_{xxxx}(x) - \mu^4 X(x) = 0. \tag{3-27}$$

The general solution to this differential equation is written in the form[38]

$$X(x) = c_1 \cosh(\mu x) + c_2 \sinh(\mu x) + c_3 \cos(\mu x) + c_4 \sin(\mu x). \tag{3-28}$$

There are now five constants which must be found to solve this differential equation (c_1, c_2, c_3, c_4, and μ).

In order to solve for μ, the general solution to the differential equation as given by Eq. 3-28 is applied to the four homogeneous boundary conditions. This yields a series of equations of the form

$$[A]\{c_i\} = \{0\} \tag{3-29}$$

where [A] is a 4x4 matrix whose elements are a function of μ and $\{c_i\}$ is a column vector of the unknown coefficients c_1, c_2, c_3, and c_4. Nontrivial solutions of this equation exist if and only if the determinant of the matrix [A] is zero. Setting the determinant to zero, and solving for μ leads to the following approximate solutions for the n eigenvalues, μ^n:

$$\mu^0 = 0$$

$$\mu^n = \frac{\pi}{4L} + \frac{\pi}{2L} n \text{ for } n = 1,2,3,.... \tag{3-30}$$

The exact values of these eigenvalues were then found numerically using Newton's method.

For each eigenvalue, there are four associated constants, c_i. It is possible to rewrite the first three of these (c_1, c_2, and c_3) in terms of the fourth (c_4). This leads to the following form of Eq. 3-28 for each of the n eigenvalues:

$$X^n(x) = c_4^n F(\mu^n, x) \text{ for } n = 1,2,3,... \tag{3-31}$$

where

$$F(\mu^n, x) = f_1^n(\mu^n)\cosh(\mu^n x) + f_2^n(\mu^n)\sinh(\mu^n x) + f_3^n(\mu^n)\cos(\mu^n x) + \sin(\mu^n x)$$

and

$$f_1(\mu) = \frac{\cos(\mu L)}{\sinh(\mu L)}\left[\frac{\cosh(\mu L)\sin(\mu L) - \cos(\mu L)\sinh(\mu L)}{\cosh(\mu L)\sin(\mu L) + \cos(\mu L)\sinh(\mu L)}\right]$$

$$f_2(\mu) = \frac{\sin(\mu L)}{\sinh(\mu L)}$$

$$f_3(\mu) = \frac{\cosh(\mu L)}{\sinh(\mu L)}\left[\frac{\cosh(\mu L)\sin(\mu L) - \cos(\mu L)\sinh(\mu L)}{\cosh(\mu L)\sin(\mu L) + \cos(\mu L)\sinh(\mu L)}\right]$$

Special attention is necessary to determine the solution for $X^0(x)$, which must have a constant value since μ^0 is applied to the general solution given by Eq. 3-28. The constant value of $X^0(x)$ will be called c_4^0. Therefore, the function $F(\mu^0,x)$ is defined to be equal to one.

The remaining constant, c_4, is found by using the initial condition and the property that each of the homogeneous solutions are orthogonal in the domain $-L \le x \le L$. This leads to the following relation

$$\int_{-L}^{L} X^n(x)X^m(x)dx = \int_{-L}^{L}\left[g(x) - \frac{x^2}{2\rho}\right]X^m(x)dx. \tag{3-32}$$

For $n \neq m$, the left-hand side of Eq. 3-32 must equal zero. Therefore, when $n = m$, a solution for c_4 for each of the n eigenvalues is found as follows:

$$c_4^n = \frac{\int_{-L}^{L}\left[g(x) - \frac{x^2}{2\rho}\right]F(\mu^n,x)dx}{\int_{-L}^{L}F(\mu^n,x)^2dx}. \tag{3-33}$$

The solution for ν in terms of μ, taken from Eq. 3-26, is given by:

$$\nu = \frac{\alpha\mu^4}{\mu^4 + \beta}. \tag{3-34}$$

With the solutions to μ^n and $c^n{}_4$ (and therefore also to ν^n), it is possible to write the final solution to the inhomogeneous partial differential equation (Eq. 3-18) as follows:

$$u(x,t) = \sum_{n=0}^{\infty} c_4^n F(\mu^n,x)e^{-\lambda^n t} + \frac{x^2}{2\rho}. \tag{3-35}$$

An analogous derivation may be used to model a linear elastic beam on a viscoelastic foundation represented as a three-parameter solid. This solution is given in Appendix B.

The deflection given by $u(x,t)$ in Eq. 3-35 includes both the extension due to the elastic response of the spring, $u_e(x,t)$, and the deflection due to the flow of the dashpot, $u_f(x,t)$. A marching scheme may be employed to relate the deflection at time t_i, $u(x,t_i)$, to the deflection at time t_{i+1}, $u(x,t_{i+1})$, in terms of the constants associated with the Maxwell model (E_o and η) and the adhesive thickness (h) as follows:

$$\frac{u(x,t_{i+1})}{h} = \frac{u(x,t_i)}{h} + \frac{\sigma_{i+1}\Delta t}{\eta} + \frac{\sigma_{i+1} - \sigma_i}{E_o}, \tag{3-36}$$

where

$$\sigma_i = \frac{E_o u_e(x,t_i)}{h} \text{ and}$$

$$\Delta t = t_{i+1} - t_i.$$

The stress, σ_i, refers to the stress along the bond length at time t_i. The definition given here, similar to that given in Eq. 3-16, differs in that the deflection due to flow must be first subtracted from the total deflection so that only the elastic response of the spring component is considered. Eq. 3-36 is rewritten to solve for $u_e(x,t)$ as follows:

$$u_e(x,t_{i+1}) = \frac{u(x,t_{i+1}) - u(x,t_i) + u_e(x,t_i)}{\frac{E_o \Delta t}{\eta} + 1}. \tag{3-37}$$

The marching scheme assumes that over some time increment Δt the stress remains constant as both the spring and dashpot elements deform. The solution obtained from Eq. 3-35 is used in Eq 3-37 to determine $u_e(x,t)$ and, therefore, $u_f(x,t)$.

As was previously mentioned, an infinite number of modes must be used to perfectly define the solution (Eq. 3-35). Only the even shaped modes have any significant effect on the final solution; the beam problem is symmetric. In addition, the magnitude of the mode shapes continually decreased for increasing eigenvalues. In the following analyses, the first seven even modes were used since these were sufficient to adequately model the beam deflection without the solution becoming unstable.

3.3.2 Uniqueness of the Solution

To demonstrate that the solution obtained for a given differential equation is meaningful, it is necessary to address the question of the uniqueness of the solution. In order to show that there exists a unique solution to this problem, and therefore that the solution given by Eq. 3-35 is unique, it is first assumed that two solutions to the original partial differential equation exist. If these solutions are defined as $u_1(x,t)$ and $u_2(x,t)$, then the sum and the difference of these solutions must also be solutions of the differential equation. The difference of these solutions is defined as U(x,t), where

$$U(x,t) = u_1(x,t) - u_2(x,t). \tag{3-38}$$

Therefore, if it can be shown that U(x,t) must identically equal zero then it follows that there can exist only one unique solution to the given partial differential equation.

It is first necessary to multiply the original partial differential equation (Eq. 3-18) by U(x,t) and integrate over the domain of x from -L to +L in the following manner:

$$\int_{-L}^{L} U\partial_t U_{xxxx}dx + \alpha\int_{-L}^{L} UU_{xxxx}dx + \beta\int_{-L}^{L} U\partial_t U dx = 0. \tag{3-39}$$

(The term ∂_t refers to a partial derivative with respect to time.) Next, integration by parts is employed to integrate the left-hand side of Eq. 3-39. To demonstrate the type of calculations required, the integration by parts will only be carried out on the first term of the equation:

$$\begin{aligned}\int_{-L}^{L} U\partial_t U_{xxxx}dx &= U\partial_t U_{xxx}\Big|_{-L}^{L} - \int_{-L}^{L} U_x\partial_t U_{xxx}dx \\ &= U\partial_t U_{xxx}\Big|_{-L}^{L} - U_x\partial_t U_{xx}\Big|_{-L}^{L} + \int_{-L}^{L} U_{xx}\partial_t U_{xx}dx\end{aligned} \tag{3-40}$$

The boundary conditions may be applied to eliminate two of the terms on the right-hand side of Eq. 3-40. Before applying the boundary conditions, they must first be rewritten in terms of U(x,t). For example, by considering that

$$u_{xx}(-L) = \frac{1}{\rho} \tag{3-41}$$

(from Eq. 3-19), it is possible to write that

$$u_{1_{xx}}(-L) = \frac{1}{\rho} \text{ and } u_{2_{xx}}(-L) = \frac{1}{\rho}. \tag{3-42}$$

Therefore, the second derivative of the function U(x,t) with respect to x, evaluated at -L may be written as

$$U_{xx}(-L) = u_{1_{xx}}(-L) - u_{2_{xx}}(-L) = 0. \tag{3-43}$$

In the same manner, the boundary conditions and the initial condition may be rewritten in terms of U(x,t) as

$$\begin{gathered}U_{xx}(\pm L) = U_{xxx}(\pm L) = 0 \text{ and} \\ U(x,0) = 0.\end{gathered} \tag{3-44}$$

By applying these boundary conditions to Eq. 3-40, the first two terms on the right-hand side are eliminated. By rewriting the final term from Eq. 3-40, the following relation may be written:

$$\int_{-L}^{L} U\partial_t U_{xxxx}dx = \frac{1}{2}d_t\int_{-L}^{L} U_{xx}^2 dx. \tag{3-45}$$

Using the integration by parts technique as described, Eq. 3-39 is written as

$$\frac{1}{2}d_t\int_{-L}^{L} U_{xx}^2 dx + \alpha\int_{-L}^{L} U_{xx}^2 dx + \frac{1}{2}\beta d_t\int_{-L}^{L} U^2 dx = 0. \tag{3-46}$$

The terms containing the derivative with respect to time, d_t, may be regrouped so that this equation may be written as

$$\frac{1}{2}\frac{d}{dt}\int_{-L}^{L}\left(U_{xx}^2 + \beta U^2\right)dx + \alpha\int_{-L}^{L} U_{xx}^2 dx = 0. \tag{3-47}$$

Since both α and β must be greater than zero (based on their definition in Eq. 3-18) and since the integral of a function squared evaluated over any domain -L to +L must be greater than or equal to zero, it is possible to conclude that the first term in Eq. 3-47 must be less than or equal to zero. This inequality is written as:

$$\frac{d}{dt}\int_{-L}^{L}\left[U_{xx}^2(x,t) + \beta U^2(x,t)\right]dx \le 0. \tag{3-48}$$

If the derivative with respect to time of a function is less than or equal to zero, then the function itself at any time must be less than or equal to the function at time zero. Since the function is the sum of the integral of a squared function (which must be greater than or equal to zero) and the product of a positive constant and the integral of another squared function (which must also be greater than or equal to zero), the function itself must be greater than or equal to zero. This set of inequalities is written as:

$$0 \le \int_{-L}^{L}\left[U_{xx}^2(x,t) + \beta U^2(x,t)\right]dx \le \int_{-L}^{L}\left[U_{xx}^2(x,0) + \beta U^2(x,0)\right]dx. \tag{3-49}$$

Equation 3-44 shows that the function evaluated at time zero must identically equal zero for any value of x within the domain of -L to +L. Therefore, the inequality may be written as:

$$0 \le \int_{-L}^{L}\left[U_{xx}^2(x,t) + \beta U^2(x,t)\right]dx \le 0, \tag{3-50}$$

so that U(x,t) must be identically equal to zero.

By proving that U(x,t) must be identically equal to zero for any time and for any value of x over the domain -L to +L, it is proven that there exists one and only one solution to the given partial differential equation.

3.3.3 Results of the Analysis

Although the primary use of this solution will be to make predictions regarding rate of debond in the curvature mismatch test systems, some preliminary results from the beam on viscoelastic foundation solution are presented here to provide further insight into the mechanics of the adhesively bonded system. The sample case to be analyzed is that presented in Section 3.2, but the adhesive is now modeled using the Maxwell element. For this case, the following material properties and geometries were used:

- $E = 210$ GPa (modulus of steel adherend)
- $t = 0.254$ mm (thickness of adherend)
- $E_o = 1.22$ MPa (spring constant of the adhesive model)
- $\eta = 30$ MPa-s (dashpot constant of the adhesive model)
- $h = 1.14$ mm (thickness of the adhesive)
- $w = 12.7$ mm (width of adherend and adhesive)
- $\rho = 35$ mm (radius of the difference in curvature between the adherend and the substrate)

The results are shown in Figs. 3.9 and 3.10. In these plots, the curves show the deflection of the beam versus beam length for discrete times ranging from time equals zero to time equals infinity. In the former case, the solution obtained here is identical to the elastic solution shown in Fig. 3.8, since this case is the initial condition. In the latter case, at time equals infinity, the beam has deflected to its original stress-free shape as given by Eq. 3-5. Note that the scales of the two figures have been altered to make the deflected shape at smaller times visible. The shape of the beam at $t = 2000$ s is present in both figures.

Obviously, this solution does not take into account a failure mechanism. This solution also does not account for the thickness of the adhesive; it is impossible for the beam to deflect into the substrate and as the predicted deflection approaches the substrate thickness assumptions regarding the behavior of the adhesive would be violated. Since the adhesive is modeled as a viscoelastic fluid, deformations grow far beyond what is realistically expected.

The results shown in both Figs. 3.9 and 3.10 represent the sum of deformations due to the spring and the dashpot components of the Maxwell model. Using the techniques described earlier (Eq. 3-37), it is possible to show the deflection associated only with the

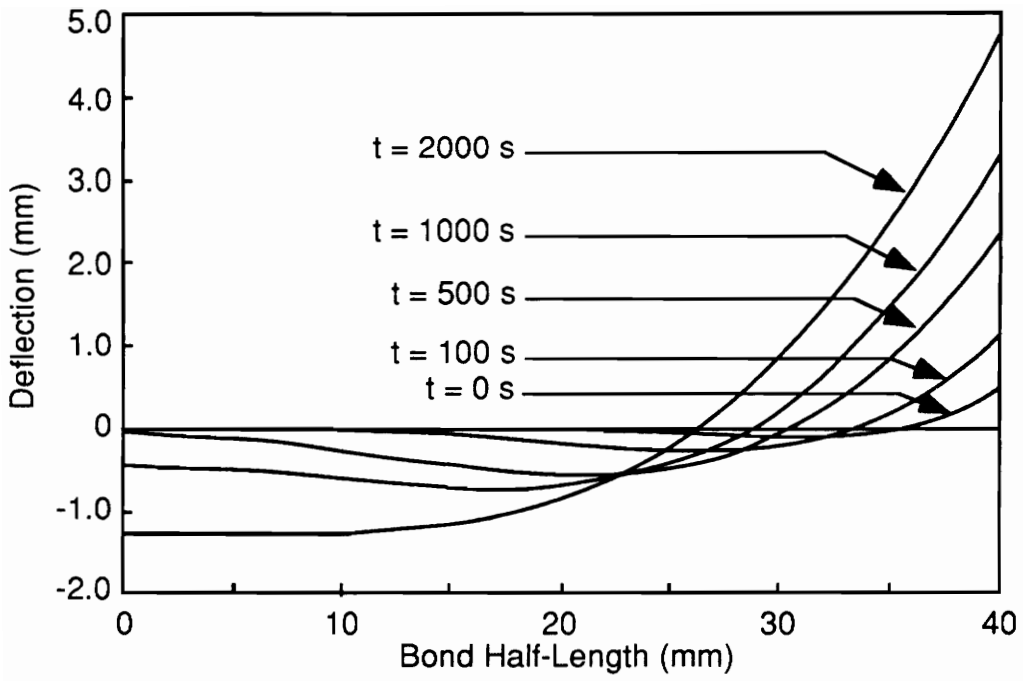

Figure 3.9 - Beam deflection up to times of 2000 s.

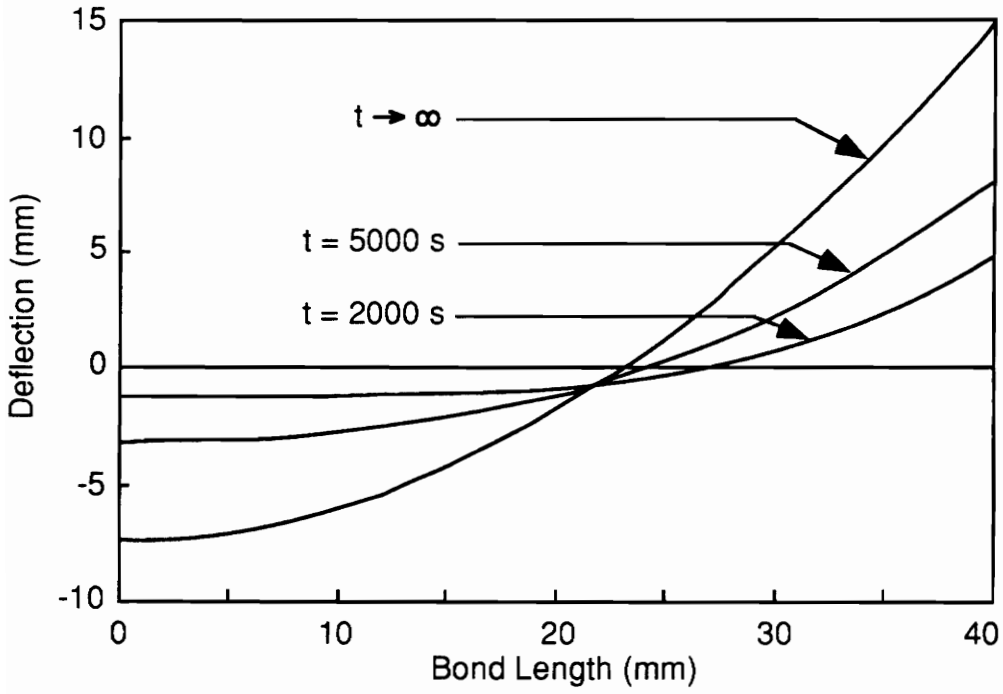

Figure 3.10 - Beam deflection at times of 2000 s and greater.

elastic spring component of the Maxwell model, u_e, for various times. These results are presented in Fig. 3.11. The shape associated with t = 0 s corresponds exactly to the initial shape of the beam as shown in Fig. 3.9, since this shape represents the instantaneous response of the beam to a given loading. As time increases, the overall elastic deformations, and therefore the stresses as well, decrease. They ultimately approach zero as time goes to infinity. These results suggest that, even after relatively short periods of time, the stress within the bond line becomes quite small for this particular system. (In this model, $\Delta t = 1$ s.)

3.3.4 Determining Rate of Debond

To numerically approximate the debond rate of an adhesively bonded system modeled using the beam on a viscoelastic foundation solution, it is necessary to introduce a failure mechanism as well as a discretization of the beam into finite lengths. A failure mechanism is required to determine when the adhesive at the endpoint of the beam begins to debond. A discretization is required so that each element, as it becomes the new endpoint, may eventually fail and the entire beam may be thus modeled to debond over time.

As was mentioned in Section 3.1, the failure mechanism chosen for this study is an ultimate extension of the adhesive based on an ultimate strain. The debonding proceeds from the endpoint of the beam where the deflection is largest. The solution to the partial differential equation is used to solve for the time required for the endpoint of the beam to reach a critical value. This is accomplished numerically using Newton's method to find the time at which the endpoint deflection equals the ultimate deflection, $u(L,t_c) = h\,\varepsilon_u$ (where t_c is the critical time and h is the adhesive thickness). In this work, the half-length beam was divided into 80 equal elements, each 0.5 mm in length.

When the critical time is found, the marching technique described in Section 3.3.2 may be used to obtain the deformations associated with both the spring, u_e, and the dashpot, u_f. When the endpoint beam segment is removed, representing debonding of that segment, the instantaneous response of the beam must be modeled using only the elastic component of the Maxwell model. In other words, when one element is removed, the stress which is dependent only on u_e must be allowed to equilibrate. This may be modeled by representing $u_e(x)$ with a Winkler beam, shortening the beam by the length of the

debonding segment, and calculating the resulting deflection for the shortened beam. The new deflected shape of the shortened beam may be obtained as follows:

$$u|_{short} = u_f + u_e|_{short} = u - u_e + u_e|_{short}, \tag{3-51}$$

where $u|_{short}$ is the deflected shape of the shortened beam, u_f is the deflected shape of the beam due solely to flow of the dashpot, u_e is the deflected shape of the beam due to the spring component before the beam is shortened, and $u_e|_{short}$ is the deflected shape of the shortened beam due to the spring component.

Equation 3-51 represents the new initial condition so that the same procedure may be repeated, i.e. solving the partial differential equation, determining the critical time at failure, shortening the beam, and obtaining a new deflected beam shape. It is suggested that the shape obtained from Eq. 3-51 be modeled using a Fourier series in the following form:

$$u|_{short} = \sum_{k=1}^{n}\left[a_k \sin\left(\frac{k\pi x}{l_s}\right) + b_k \cos\left(\frac{k\pi x}{l_s}\right)\right], \tag{3-52}$$

where l_s is the shortened length of the beam and a_k and b_k are coefficients which must be numerically found to model the beam shape. As the new initial condition, this function would replace g(x) given in Eq. 3-20. By following this procedure, the debond rate may be numerically approximated from the slope of the curve of debond length versus time.

In addition to requiring that the beam be discretized into finite lengths, it is also necessary to assume that maximum extension is an adequate failure mechanism and that the deflected shape of the shortened beam (after debonding) is appropriately modeled by the technique described. In subsequent analyses, another assumption is introduced regarding the modeling of the deflected shape of the shortened beam. From Fig. 3.11, the magnitude of u_e is shown to decrease over time, approaching zero. Instead of following the procedure previously outlined to determine the shape of the shortened beam, two conditions representing two extreme cases will be used to provide an upper and lower bound on the predicted debond rate for the experimental systems. The lower bound is obtained by assuming that there is no significant instantaneous response of the beam due to the shortening of the beam during debonding. The experimental results would tend to approach this case for lower debond rates. The upper bound is obtained by assuming no change in the elastic response of the Maxwell model over time, except due to changes of the beam length. Experimental results would approach this case for higher debond rates.

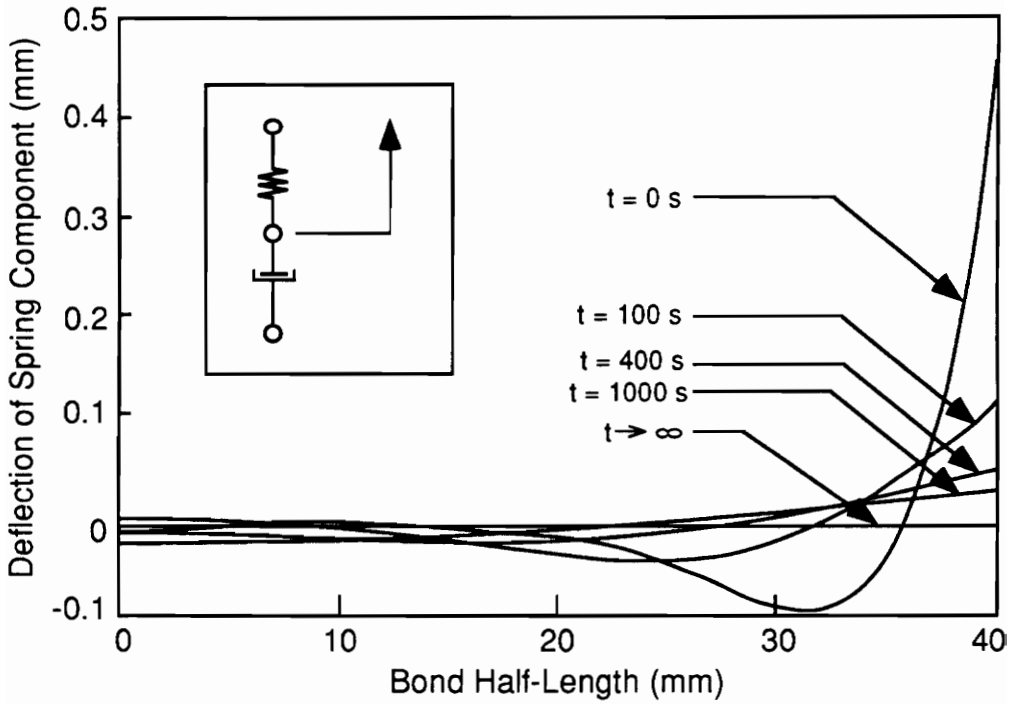

Figure 3.11 - Deflection of spring component of Maxwell model over time.

From Fig. 3.11, it is apparent that the actual behavior of the system is somewhere between the predictions obtained from these two assumptions.

For the lower bound assumption, the final deflected shape of the shortened beam is simply obtained by removing the end segment from the deflected shape of the beam at the critical failure time. Since there is no elastic response, nothing else must be done.

For the upper bound assumption, the elastic response as described by the beam on elastic foundation solution must first be subtracted from the deflected shape at the critical failure time. The elastic response of the shortened beam is then added back to obtain the final deflected shape of the shortened beam. This is similar to Eq. 3-51, except no marching scheme is employed to determine the elastic component of the total deformation. Instead, since it is assumed that there is no change in the elastic response of the Maxwell model, the original solution to the beam on elastic foundation problem is used to determine the elastic response based on the length of the beam before and after debonding.

The shape of the shortened beam, for both the upper and lower bound solutions, is fitted with Eq. 3-15 by determining the appropriate constants, λ and ρ. This is done to simplify the function representing the deflected shape of the shortened beam by putting it in a form which is more easily solved using numerical methods. The implications of this assumption will be discussed in Section 3.7.

3.3.5 Results of Rate Analysis

Sample results are presented from the recursive solution technique described in Section 3.3.4 regarding debonding of an adherend (the same system is used here as well as in Sections 3.2.2 and 3.3.3). The ultimate strain used was 0.835, corresponding to a maximum extension of 0.951 mm. Figure 3.12 shows the deflected shape of the same beam at various times. Unlike the results presented in Figs. 3.9 and 3.10, a failure mechanism is incorporated into these results. The elastic foundation solution, which is also the initial condition, is shown. As time increases, this shape changes while the endpoint deflection continues to increase. When the endpoint deflection reaches the maximum deflection, that element fails and the beam debonds, with the debond propagating from right to left in the figure.

Although this information is valuable, additional information may be obtained by plotting the data as shown in Fig. 3.13. In this figure, the debond length is plotted versus time for the previously discussed case, with ρ = 35 mm, and another case with identical

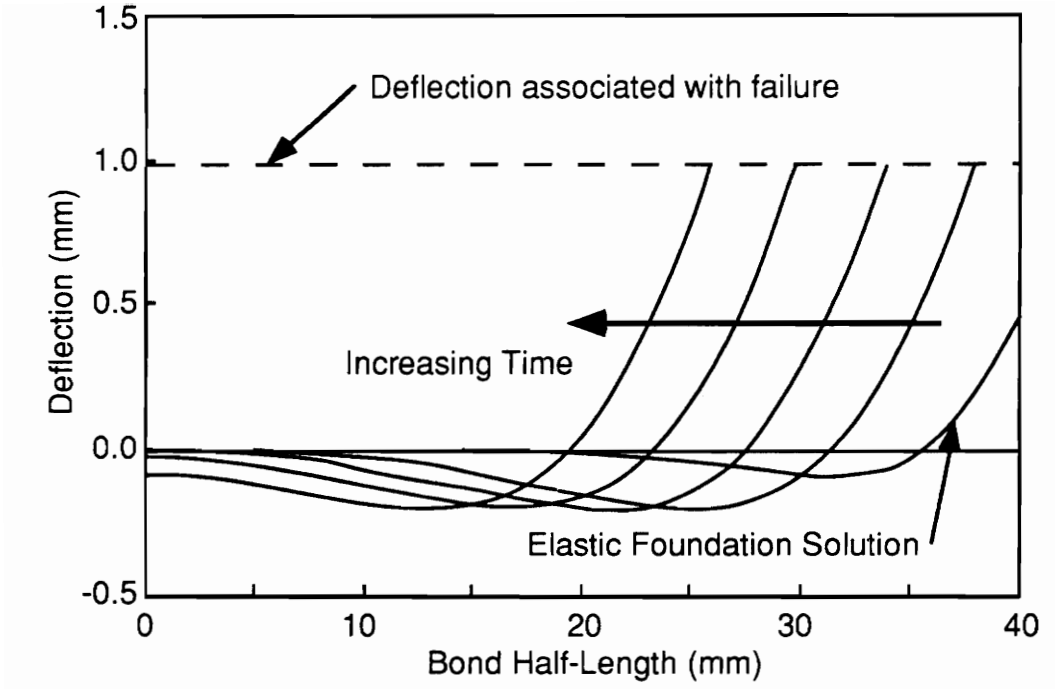

Figure 3.12 - Results showing beam deflection and debonding based on beam on a viscoelastic foundation solution.

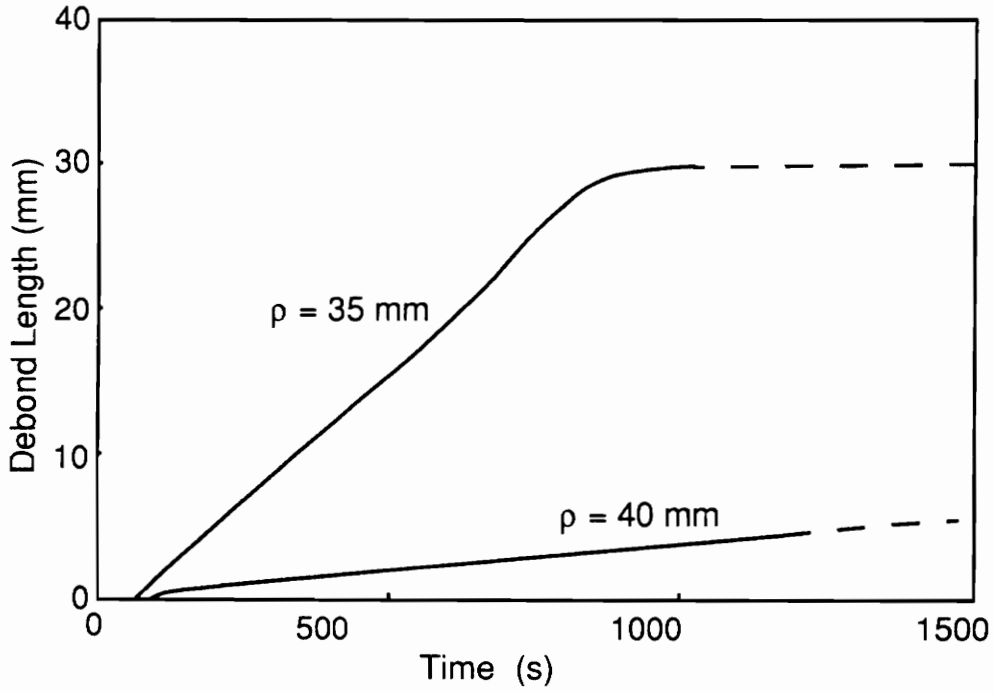

Figure 3.13 - Analytical results, using the Maxwell model, of debond versus time for cases with $\rho = 35$ mm and $\rho = 40$ mm.

material properties with $\rho = 40$ mm. (In this figure, the half length of the beam is 40 mm.) The beam was discretized into equal lengths of 0.5 mm. Three areas of interest are apparent from this figure. First, it is apparent that there is some delay in time until debonding occurs, which is different for the two cases. Second, the majority of the curve shown is nearly linear, implying that once debonding begins, debonding continues at a constant rate. Finally, as the beam becomes much shorter for the case with $\rho = 35$ mm (approximately 10 mm), the solution shows a major decrease in rate of debond. At this point, the numerical solution became very unstable, so that the current solution technique was unable to produce meaningful results. The curve on the figure is shown dashed over this range. For the second case, the numerical solution also became unstable after approximately fifteen iterations. This was most likely due to an insufficient number of modes chosen to model the system and/or inaccuracies introduced with assumptions about material behavior.

With any discretization technique, questions arise regarding the convergence of the numerically obtained solution. Since two different cases of material behavior were studied, maximum elastic response and no elastic response, two different convergence studies must be conducted. In order to gain some understanding into this question, tests were run for each case of elastic response at various beam increment lengths. The results of the convergence study, shown in Fig. 3.14, make use of the same experimental system previously described with $\rho = 35$ mm. The rates for the various beam increments were normalized by dividing the result obtained at each increment by the rate obtained when using an increment of length 0.5 mm. The increment lengths were also normalized by dividing each length by 0.5 mm. For both analytical cases, relatively large changes in rate occur as the increment length decreases. For the analytical solution with maximum elastic response, the rate results also change as the increment length becomes larger. Questions about convergence will be discussed in Section 3.7.

3.4 The Elastic-Viscoplastic Solution

Another solution technique is proposed which incorporates the Bingham model into a recursive solution which is used to predict the behavior of the same adhesively bonded systems. Initially, the stress distribution along the bond length is determined with the

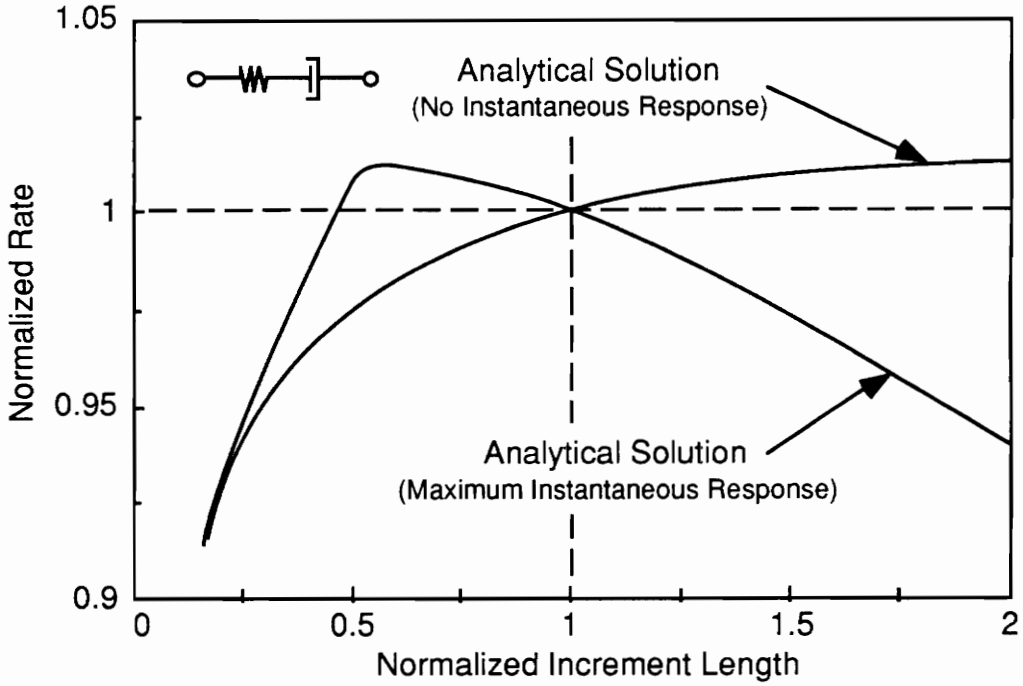

Figure 3.14 - Convergence study showing normalized rates versus normalized increment lengths for both analytical solutions.

solution to the beam on elastic foundation problem, which was discussed in Section 3.2. A recursive method is used to determine the rate of debond of the adherend from the substrate using a series of Bingham elements, assumed to model the adhesive layer. The stress distribution obtained from the beam on elastic foundation solution is then applied to the series of Bingham elements.

By applying this stress distribution, two assumptions are made. First, it is assumed that the beam is of a length great enough such that the stress distribution obtained from the elastic analysis also shifts as the debond propagates. Recalling from earlier results, as the beam becomes relatively short, the shape of the beam deflection, and therefore the stress distribution, changes.

Second, it is assumed that there is no change in the stress state due to the viscoplastic flow of the Bingham elements. For example, the stress at the endpoint obtained from the beam on elastic foundation solution is applied until the end element fails. At that time, the stress is shifted so that the same endpoint stress is now applied to the new endpoint. This assumption greatly simplifies the problem by ignoring any stress redistribution not associated with changing the beam length. The assumption becomes valid for cases with short times until failure and for cases with lower stresses, when there is less opportunity for flow.

By utilizing the Bingham model, it is not necessary to observe the effects of stress applied over time to any elements when the applied stress is less than the critical stress of the slider, σ_o. The strain resulting from a stress applied to a Bingham element over some time, t, may be expressed as

$$\varepsilon = \frac{\sigma}{E_o} + \left(\frac{\sigma - \sigma_o}{\eta} \right) t \tag{3-53}$$

where the constants of the Bingham model (E_o, η, and σ_o) are as described earlier. Equation 3-53 is rewritten in terms of the time it takes for the end element to reach a critical strain, ε_u. This time is applied to all of the Bingham elements which are subjected to a stress greater than σ_o. When the end element reaches a strain of ε_u, it is considered to have failed and the stress distribution is shifted over by one element. The same technique is continuously applied, producing the time it takes for each of the final elements to fail.

Obviously, each element with an applied stress greater than σ_o will have undergone flow produced at lower stresses for various times. This means that the complexity of the recursive solution increases as the number of elements considered also increases. If there

are N elements that are plastically deformed at any given time, then the following relation[33] holds to describe the time it takes for the ith element to fail, as measured from the time the preceding element failed:

$$t_i = \frac{\eta\left(\varepsilon_u - \frac{\sigma_1}{E}\right)}{\sigma_1 - \sigma_o} K_i, \tag{3-54}$$

where

$$K_i = 0 \quad \text{for all} \quad i \le 0 \text{ and}$$

$$K_i = 1 - \sum_{j=1}^{N-1}\left(\frac{\sigma_{j+1} - \sigma_o}{\sigma_1 - \sigma_o}\right) K_{i-j} \quad \text{for all} \quad i \ge 1.$$

The subscript applied to σ refers to each of the discrete elements represented by a single Bingham element. For example, if as shown in Fig. 3.15, the region of $\sigma > \sigma_o$ were divided into four elements that undergo plastic deformation, the values of σ_i would correspond to the stress states at the points shown. Since the stress state is simply assumed to shift as the debond propagates, the values of σ_i remain constant.

The sizing of the discretization is based on the chosen number of Bingham elements which undergo plastic deformation. This value, which must be determined to obtain the final debond rate, is a function of the length of the beam subjected to stresses greater than σ_o.

The recursive solution is applied until the analytically determined debond rate reaches a steady state. For the sample case used earlier in Section 3.3 with the following material properties:

- E = 210 GPa (modulus of steel adherend)
- t = 0.254 mm (thickness of adherend)
- E_o = 1.22 MPa (spring constant of the adhesive model)
- η = 57.6 MPa-s (dashpot constant of the adhesive model)
- σ_o = 170 kPa (slider constant of the adhesive model)
- h = 1.14 mm (thickness of the adhesive)
- w = 12.7 mm (width of adherend and adhesive)
- ρ = 35 mm (radius of the difference in curvature between the adherend and the substrate)

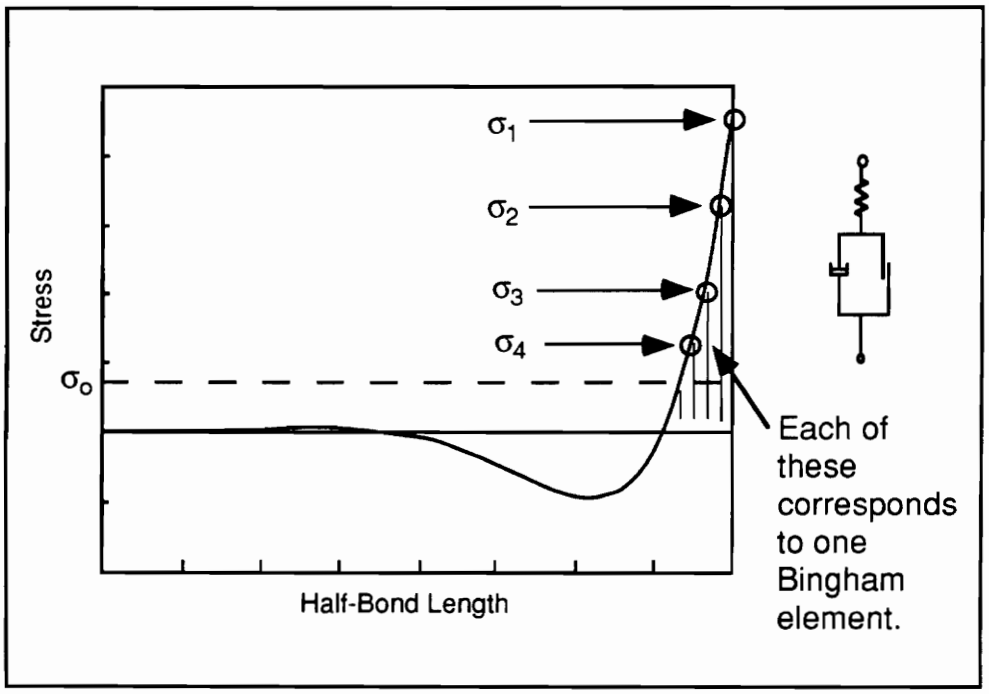

Figure 3.15 - Schematic of recursive solution using Bingham elements. five Bingham elements were considered to undergo flow at any given time (the beam was divided into segments of 0.582 mm). A debond rate of 0.0175 mm/s was predicted for this sample case.

3.5 The Experimental System

The basic geometry of the experiments to determine debond rate as a function of critical strain energy release rate for the adhesive system is shown in Fig. 3.16. A steel beam of length 2L, corresponding to a half-length of L, is bonded to a glass cylinder of radius r. The glass cylinder was grit blasted to create a roughened surface so that the adhesive would debond at the adhesive-glass interface. Before the adhesive was applied, both the glass and steel surfaces were thoroughly cleaned with acetone.

The adhesive tested was the 3M Scotch-Mount brand Y-4248 neoprene foam tape. The adhesive, on both sides of the foam liner, was the AR-7 long aging acrylic. The width (w) of both the pressure sensitive adhesive and the steel adherend was 12.7 mm, while the thickness of the adhesive (h) was 1.14 mm. Other information about the steel and the adhesive is presented in Table 3.1.

Eight different variations of the debond test were conducted by varying both the radius of the glass cylinder (r) and the thickness of the steel adherend (t). Since the radius of the difference in curvature (ρ) between the stress-free shape of the adherend and the substrate is measured to the neutral axis of the steel adherend, the value of ρ is defined as the sum of the radius of the glass cylinder (r), the adhesive thickness (h), and one-half of the thickness of the steel adherend (t). Four tests were conducted for each case.

The ultimate strain of the entire pressure sensitive adhesive is used as the failure criterion. For this particular material, the ultimate strain (ε_u) was taken to be 0.835. This leads to a maximum extension of the adhesive of 0.951 mm.

The data is presented from the debond tests by plotting the debond rate as a function of applied strain energy release rate. By assuming that as a sufficiently long adherend debonds a given increment the shape of the deflected beam near the tip does not change and by realizing that the adhesive strain energy is negligible away from the bond tip, the only strain energy available comes from the energy associated with the bending of the beam. By considering these assumptions, Dillard[30] considered the energy balance equation

$$-\delta U = G\delta A\,, \tag{3-55}$$

where δU is the energy in the beam, G is the available strain energy release rate, and δA is a unit area. The energy in the beam, δU, subjected to a radius of curvature, ρ, is defined as:

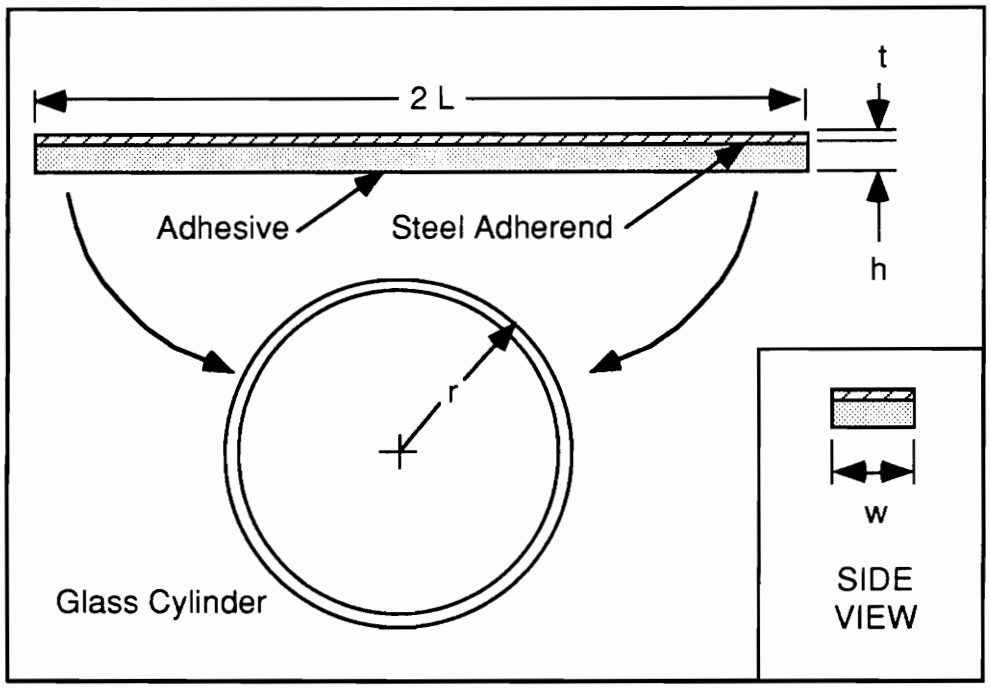

Figure 3.16 - Geometry of the debond test.

Table 3.1 Material properties of the adhesive and adherend.

Material	Property	Value
Steel	Elastic Modulus, E	210 GPa
Adhesive	Elastic Modulus, E (Spring constants in models)	1.22 MPa
	Dashpot Constant, η (Maxwell Model)	30 MPa-s
	Slider Constant, σ_o	0.17 MPa
	Dashpot Constant, η (Bingham Model)	57.6 MPa-s

$$\delta U = \frac{M^2}{2EI}\delta x = \frac{EI}{2\rho^2}\delta x, \tag{3-56}$$

where M is a bending moment (due to the curvature mismatch), EI is the bending stiffness of the beam, ρ is the radius of curvature of the beam, and δx is a unit length. Therefore, the available strain energy release rate, G, due solely to the bending of the adherend may be written as

$$G = \frac{EI}{2w\rho^2}, \tag{3-57}$$

where w is the width of the adherend.

The radius, adherend thickness, and applied strain energy release rate for the eight experimental systems are presented in Table 3.2. The eight test cases are signified as TC1 through TC8, in order of increasing applied strain energy release rate. The sample results presented in the previous sections used the values given for experimental system TC6.

After application of the adhesive to the adherend, the adherend was clamped onto the glass cylinder and held for 30 minutes with a pipe clamp. When the clamp was removed, the adherend was allowed to freely debond over time. Measurements of debond at discrete times were taken throughout the test. The tests conducted in this work were run under ambient laboratory conditions ($T \approx 22$ °C and $RH \approx 60\%$).

3.6 Results

The results section of this work includes not only the results of the debond tests, but also the results of the two analytical models of bond behavior. Figure 3.17 shows the debond length for cases TC5 and TC6 versus time. The error bars show plus and minus the standard deviation of the data taken at discrete points in time, while the dashed curves are fitted to the data points. The debond rates are determined from these results by fitting a line through the linear regions of the curves. For TC6, this region is over the range of time from approximately 1,000 s to 5,000 s. For TC5, this region is over the range of time from approximately 4,000 s to 20,000 s. For both cases, the half-length of the adherend is approximately 100 mm.

The steady-state debond rates are plotted as a function of applied strain energy release rates for the eight systems tested in Fig. 3.18. The error bars shown represent plus

Table 3.2 Geometry and applied strain energy release rates, G, of experimental systems.

Test Case	ρ (mm)	t (μm)	G (J/m^2)
TC1	40	152	18.5
TC2	60	203	19.8
TC3	60	254	38.7
TC4	35	203	57.0
TC5	40	254	85.7
TC6	35	254	111
TC7	35	305	192
TC8	27	305	318

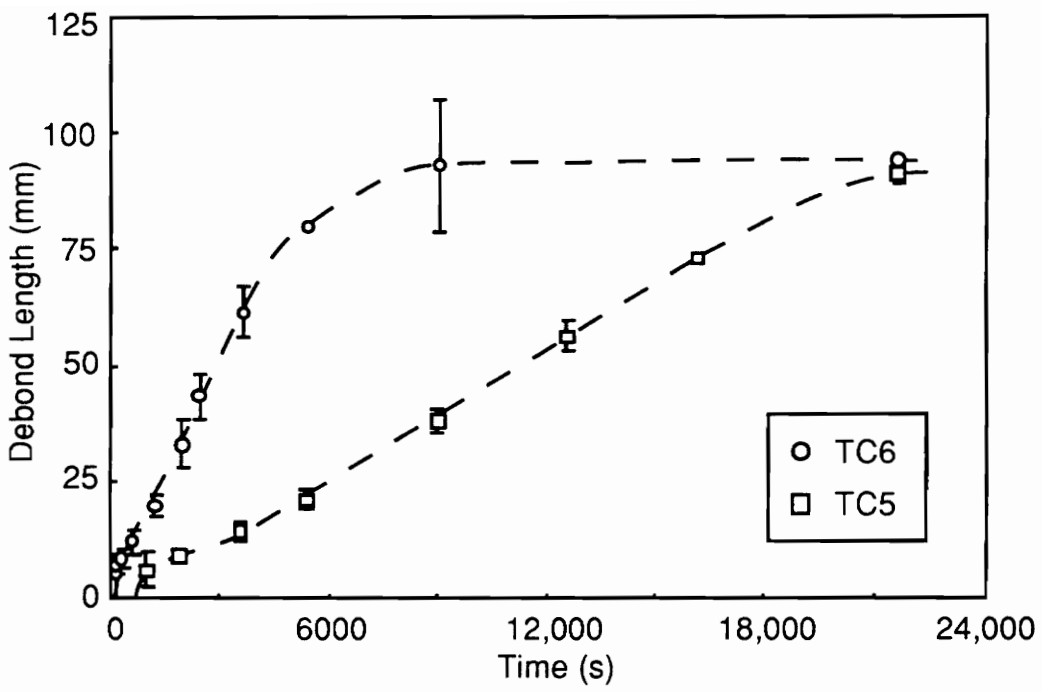

Figure 3.17 - Experimental results of debond versus time for cases TC5 and TC6.

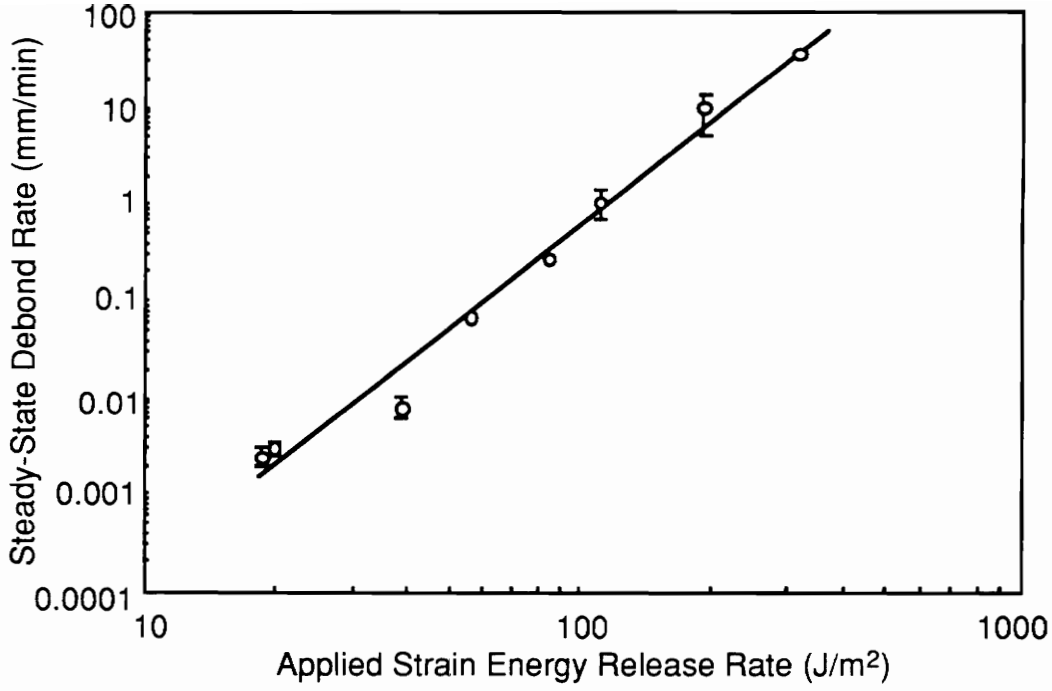

Figure 3.18 - Experimental debond rates as a function of applied strain energy release rates.

and minus the standard deviation due to experimental error. The line fitted on this log-log plot is used to compare the experimentally determined debond rates to the analytically determined rates.

Figure 3.19 shows a plot of the experimental line showing debond rate versus G and the analytically determined equivalent results using the beam on a viscoelastic foundation solution with the Maxwell element modeling the adhesive. The analytical lines represent the upper and lower bounds of debond rates based on assuming no elastic response of the adhesive to debonding and assuming the maximum possible elastic response of the adhesive. Figure 3.20 shows the results from the analytical solution using the Bingham elements. In both figures, the line fitted from the experimental results is shown dashed.

From both experimental observation and the solution given by the Maxwell model, there appears to be a delay before observable debonding begins. As another means of comparing experimental results to analytical predictions, the time to observable first debond of the adherend is shown in Fig. 3.21. The cases are shown in order from smallest to largest applied strain energy release rate due solely to the bending of the steel adherend.

During experimentation, the adhesive underwent filamentation near the bond tip. The development of a filamentation zone was a process that began when the stress was first applied to the adhesive when the experiments began. Over time, as the adherend debonded, the filamentation zone gradually increased in length. For the cased with lower debond rates (TC1 - TC6), the filamentation zone would grow until reaching a length of approximately 2 - 4 mm. For cases TC7 and TC8, the debond propagated so quickly that no observable filamentation occurred.

3.7 Discussion

Before discussing the results of the experimental and analytical work, the assumptions associated with the various models are summarized. For both the viscoelastic (Maxwell element) and elastic-viscoplastic (Bingham element) models, it was assumed that the curvature mismatch between the steel adherends and the glass cylinders could be modeled with the parabolic equation involving ρ, Eq. 3-11, over any small section. It was also assumed that beam deflections were small enough such that the adhesive would continue to behave in a linear manner. Finally, it was assumed for both cases that a single

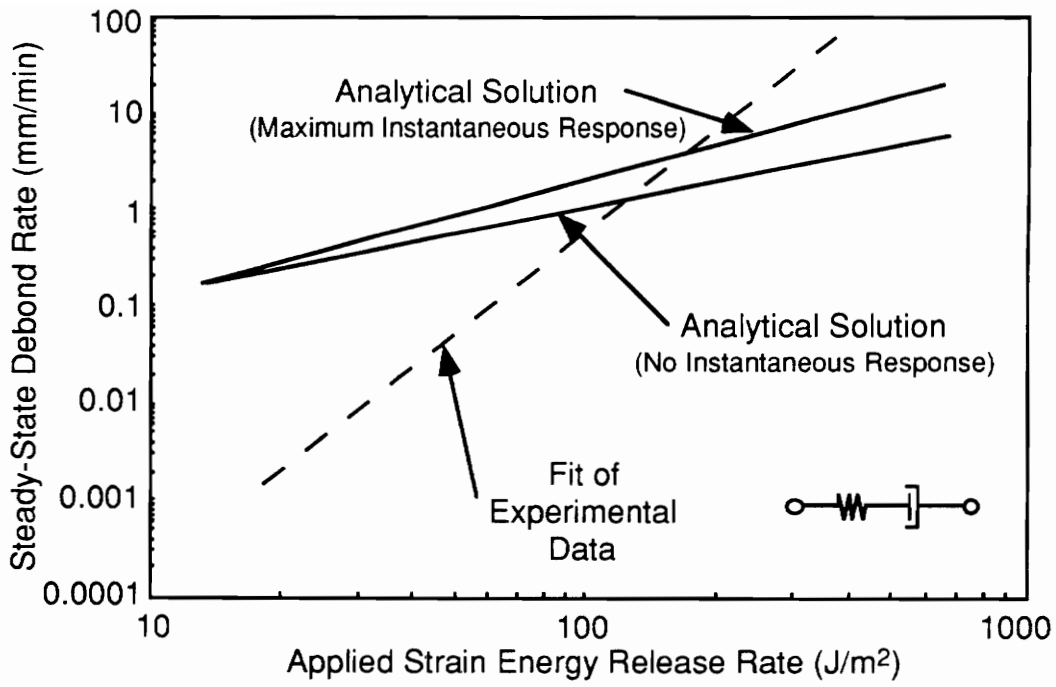

Figure 3.19 - Predicted debond rates and experimental rates as a function of applied strain energy release rates, G, using the Maxwell model.

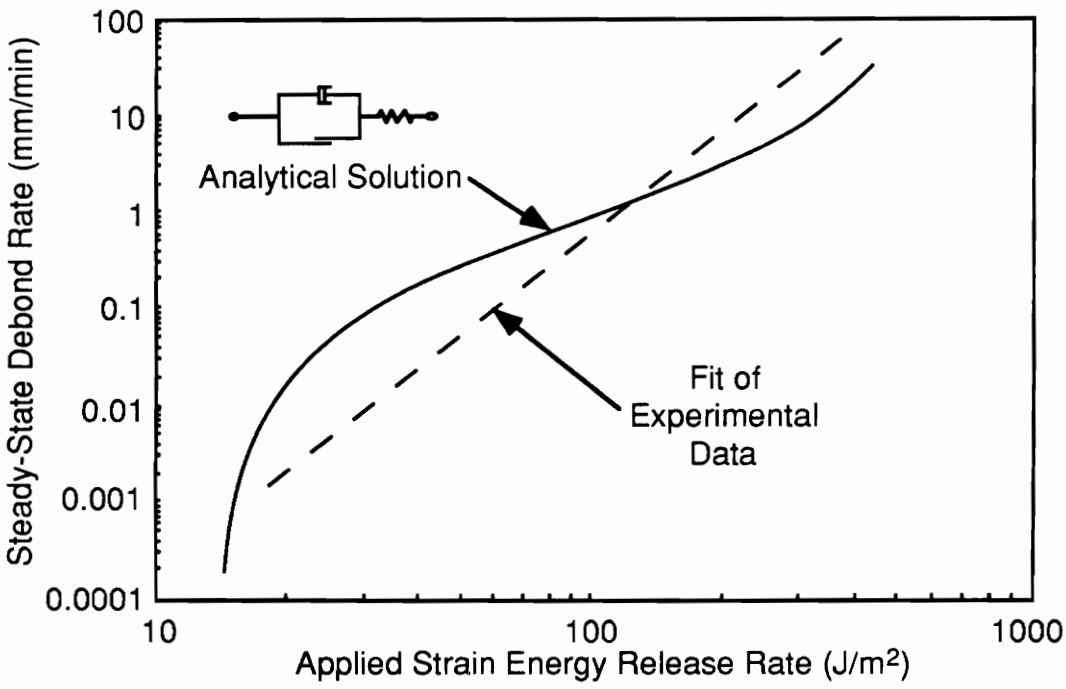

Figure 3.20 - Predicted debond rates and experimental rates as a function of applied strain energy release rates, G, using the Bingham model.

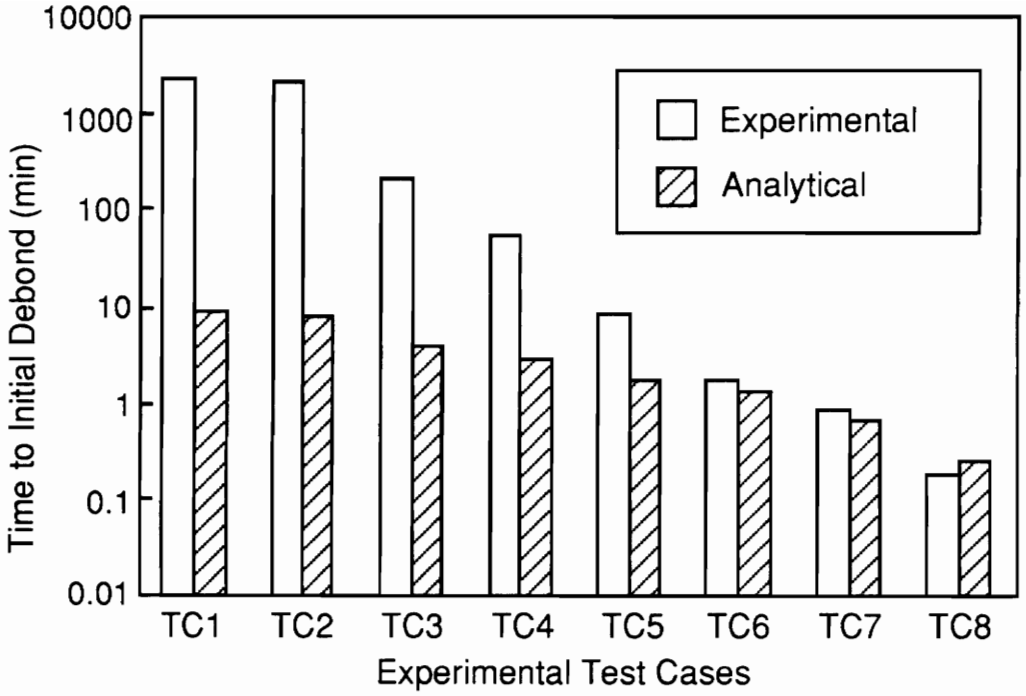

Figure 3.21 - Time to initial debond from experimental and analytical results.

failure criterion of ultimate strain, independent of strain rate, would adequately model the adhesive's behavior. There is no evidence to suggest that these assumptions might lead to any deviation between experimental and analytical results.

A number of additional assumptions were made for the viscoelastic model. First, the Maxwell model of the adhesive is limited to the linear region of the adhesive's response to loading. Since this region is only valid over a portion of the material's response to loading before failure occurs, the nonlinear portion of the adhesive behavior is modeled incorrectly. For the tests at lower debond rates, this nonlinear region is a relatively larger portion of the total material response until failure when compared with the tests at higher debond rates.

As was discussed in Section 3.3.4, the response of the beam to debonding is not accurately modeled. Rather, two extreme cases of its behavior are used to establish an upper and lower bound on the debond rate results.

It was also assumed that the discretization of the beam into finite lengths would allow for converging solutions. From the results shown in Fig. 3.15, this assumption is somewhat questionable. For the analytical solution assuming negligible elastic response to debonding, the changing rate for decreasing the beam increment length may be explained by considering that for shorter time intervals the elastic response becomes more significant. Therefore, for shorter increment lengths, the beam deformation is not accurately modeled and the solution is less likely to converge. The curve showing normalized rate versus normalized increment length in Fig. 3.15 for the maximum elastic response case is more difficult to explain. It suggests that for large length increments, and for longer time increments, the elastic response of the adhesive is over-represented by the model. For shorter increments, it would be expected that this assumption is valid, though. It is possible that the sudden changes in rate for decreasing increment length may be due to numerical errors.

It is also possible that the lack of convergence may be due to the way in which the problem has been defined. This question should be further addressed in any future work before utilizing the method presented within this thesis. It is possible that some physical phenomena have not been properly accounted for in the analytical solution. For example, it is assumed that when the beam endpoint reaches a critical extension, a length of the beam corresponding to the discretization length simultaneously debonds. Depending on the discretization length, this may not be a valid assumption.

The assumptions made regarding the elastic-viscoplastic solution also deal with the adhesive model and with the debond model. It was assumed that the stress-strain tests which were conducted at the lower strain rates could be used to model the adhesive behavior at infinitesimal strain rates. If this assumption were not valid, the results obtained for lower debond rates would be questionable. For example, the model predicts that some lower bound of applied stress exists for which no extension of the dashpot element will occur. If this yield strength were too high, the model would predict lower debond rates.

It was also assumed that the stress distribution obtained from the elastic solution would adequately model the experimental system and that the stress distribution would simply shift as the beam debonded. This model assumes no decrease in the stress as a result of viscoplasticity. Instead, the same stress profile is simply applied until failure of the end segment, at which time the stress profile is shifted by one segment. Any reduction in stress due to the viscoplastic flow of the adhesive would tend to decrease the debond rate. Therefore, this assumption tends to predict higher rates of debond. With this assumption in mind, the elastic-viscoplastic technique presented must be considered as a rather simplistic method for approximating debond rates. It is included only as an alternative method to the beam on a viscoelastic foundation method.

Based on a comparison of the two analytical models with the experimental results, a number of conclusions may be drawn. The model using the Maxwell element demonstrates the delayed debond of the adherend, a large nearly linear region suggesting constant debond rate, and the effect of approaching the mid-point of the beam when the debond rate is observed to greatly decrease. The model does not account for the nonlinear debond length versus time observed experimentally in the beginning of testing. Physically, this nonlinear behavior is due most likely to the slow development of the filamentation zone.

The Maxwell model also predicts much higher debond rates for the lower applied strain energy release rate systems. This is also reflected in the results showing the time to initial debond. The debond rate predictions for the higher values of applied G (TC7 and TC8) are conversely too low. In addition to the assumptions previously mentioned, two other sources of error between observed experimental and analytical results are suggested. First, the adhesive developed filamentation zones which were not accounted for in the model. These zones, more pronounced for the lower debond rates, are expected to act as stress reducers at the bond tip. Reducing stress would tend to decrease debond rate. Second, the numerical solution became increasingly unstable for cases with lower applied

strain energy release rates. It is possible that there is greater numerical error introduced into the solutions obtained for the lower debond rates.

The predicted debond rates obtained from the Bingham model behave similarly to material properties which are modeled using the Paris Law. The lower bound of G for which no debonding will occur (between 10 and 20 J/m^2) is due to the value used for yield strength. In addition to the assumptions previously discussed regarding this model, adhesive filamentation is not modeled by this approach either. As before, any reductions in stress due to adhesive filamentation would tend to reduce debond rates.

The experimental results give some additional insight into the analytical predictions obtained by both the Maxwell element and Bingham element models. Experimental results demonstrate the need for an accurate model of the adhesive. The greater deviation associated with the Maxwell element model may be attributed to the greater degree of inaccuracy in modeling this particular adhesive with Maxwell elements. The results also suggest that the gross deformations associated with the filamentation of the adhesive may be too great to account for within the elastic or viscoelastic solutions; it may be necessary to specifically introduce stress reduction zones to represent this phenomenon. Additional work incorporating the effects of adhesive filamentation would be necessary to improve the modeling technique[39,40,41]. It may also be true in this system that a single failure mechanism of ultimate strain may be insufficient to represent failure[42]. It may be necessary to investigate this further to develop a comprehensive failure mechanism that is rate dependent, for example.

4.0 SUMMARY AND FUTURE WORK

An improved understanding into the mechanisms of cling between thin polymeric films and a variety of substrates is obtained, based on analyses of material properties and results from peel testing. Experimentally determined values of energy associated with the work of adhesion, through contact angle tests, and the total debonding energy, through peel tests, were conducted. Surface roughness was a dominant factor influencing cling between film and substrate, due primarily to its impact on both wetting and contact electrification. Under the test conditions of this study, the poly(vinyl chloride) film exhibited superior cling to the substrates studied. This may be due to increased electrostatic attractive forces acting on the polar PVC film within a process zone near the crack tip. Increased energy of debonding may also be due to differences in rate effects on this particular film.

Additional experiments may be conducted to improve understanding about the effects of rate on measured debonding energy. Tests may also be conducted which study gross plastic deformation on both the mechanisms of adhesion and the energy associated with debonding films from their substrates. Although many insights have been gained into the effects that various adhesive mechanisms and factors have on debonding energy, there is still much room to extend this work to better understand cling of polymeric films.

Experiments have been conducted to study the relationship between debond rate and applied strain energy release rate of curvature mismatch systems. The debond tests used for this study have been modeled by two different analytical techniques: the beam on a viscoelastic foundation solution and the elastic-viscoplastic model. The derivations of both solution techniques have been presented. Experimental results show that these techniques accurately portray certain aspects of bond behavior, although there are limitations as well. These limitations are likely due to a combination of inaccurate modeling of the adhesive, physical phenomena which are unaccounted for within the current solutions, limiting assumptions about material behavior, and numerical errors.

Therefore, additional work is recommended for refining numerical techniques to improve the solution and accounting for filamentation of the adhesive within the models. It is also important to determine the source of the lack of convergence of the solution using the discretization technique, Section 3.7. The flow of the Maxwell element may also be accounted for by improving the debond prediction technique, as discussed in Section

3.3.4. A more detailed failure mechanism may also be introduced to improve debond predictions. Due to the difficulties in using a closed form solution, it may be necessary to develop a numerical solution to this problem, e.g. a finite difference or a finite element method.

Since the fundamental analytical work has been completed for the curvature mismatch problem, it is possible to use the results obtained from this work and begin experimentation with adhesives, e.g. comparing different adhesives or testing under a variety of environmental conditions. It is also possible to extend this work to more sophisticated viscoelastic models using similar procedures, although the mathematics would become increasingly more difficult.

REFERENCES

1. R.J. Farris and J.L. Goldfarb, *J. Adh. Sci. Technol.*, **7**, 853-868 (1993)
2. S. Lee, L.C. Jensen, S.C. Langford, and J.T. Dickinson, *J. Adh. Sci. Technol.*, **9**, 1-26 (1995)
3. V. Mangipudi, M. Tirrell, and A.V. Pocius, *J. Adh. Sci. Technol.*, **8**, 1251-1270 (1994)
4. H.G. VanHarrach and B.N. Chapman, *Thin Solid Films*, **13**, 157-161 (1972)
5. J.N. Israelachvili, *J. Vac. Sci. Technol. A*, **10**, 2961-2967 (1991)
6. J.N. Israelachvili, *Intermolecular and Surface Forces*, Academic Press, London (1985)
7. E.H. Andrews and A.J. Kinloch, *Proc. R. Soc. Lond. A*, **332**, 385-399 (1973)
8. J.T. Dickinson, L.C. Jensen, S. Lee, L. Scudiero, and S.C. Langford, *J. Adh. Sci. Technol.*, **8**, 1285-1309 (1994)
9. L. Scudiero, J.T. Dickinson, L.C. Jensen, and S.C. Langford, *J. Adh. Sci. Technol.*, **9**, 27-45 (1995)
10. A.D. Roberts, *J. Phys. D: Appl. Phys.*, **10**, 1801-1819 (1977)
11. R.G. Horn and D.T. Smith, *Science*, **256**, 362-364 (1992)
12. D.A. Hays, in *Fundamentals of Adhesion*, L.H. Lee (ed), Plenum Press, New York (1991)
13. C.B. Duke and T.J. Fabish, *J. Appl. Phys.*, **49**, 315-321 (1978)
14. J. Lowell and A.C. Rose-Innes, *Advances in Physics*, **29**, 947-1023 (1980)
15. T.J. Fabish, H.M. Saltsburg, and M.L. Hair, *J. Appl. Physics*, **47**, 940-948 (1976)
16. J.D. Cobine, *Gaseous Conductors*, McGraw-Hill Book Company, New York, 172-176 (1941)
17. H.T. Stokes, *Solid State Physics*, Allyn & Bacon, Newton, MA, 128-131 (1987)
18. A.N. Gent and G.R. Hamed, *J. Appl. Polymer Sci.*, **21**, 2817-2831 (1977)
19. K.S. Kim and J. Kim, *J. Eng. Mat. Technol.*, **110**, 266-273 (1988)
20. M.D. Thouless and H.M. Jensen, *J. Adhesion*, **38**, 185-197 (1992)
21. Z. Suo and J.W. Hutchinson, *Int. J. Fracture*, **43**, 1-18 (1990)
22. J.G. Williams, *J. Adhesion*, **41**, 225-239 (1993)
23. W.R. Salaneck, A. Paton, and D.T. Clark, *J. Appl. Physics*, **47**, 144-147 (1976)

24. E.J. Berger, *J. Adh. Sci. Technol.*, **4**, 373-391 (1990)
25. G.P. Anderson, S.J. Bennett, and K.L. DeVries, *Analysis and Testing of Adhesive Bonds*, Academic Press, New York, 82-85 (1977)
26. D.W. VanKrevelen, *Properties of Polymers: Their Estimation and Correlation with Chemical Structures*, Elsevier Scientific Publishing Company, New York, 152-154 (1976)
27. A.J. Kinloch, *Adhesion and Adhesives: Science and Technology*, Chapman and Hall, London, 26 (1995)
28. Conversation with Dr. J.P. Wightman, June 1996
29. *Concise Encyclopedia of Polymer Science and Engineering*, J.I. Kroschwitz (ed), Wiley, New York, 351 (1990)
30. D.A. Dillard, *J. Adhesion*, **26**, 59-69 (1988)
31. T.A. Corson, Y. Lai, and D.A. Dillard, *J. Adhesion*, **33**, 107-122 (1990)
32. I.W. Flügge, *Viscoelasticity*, Springer-Verlag, New York, 1-94 (1975)
33. H.F. Brinson, in *Deformation and Fracture of High Polymers*, H.H. Kausch, J.A. Hassell, and R.I. Jaffee (eds), Plenum Press, New York (1972)
34. M. Hetényi, *Beams on Elastic Foundations*, Ann Arbor: University of Michigan Press (1946)
35. A.P. Boresi, R.J. Schmidt, and O.M Sidebottom, *Advanced Mechanics of Materials,* John Wiley and Sons, Inc., New York, 404-426 (1993)
36. H. Kobayashi and K. Sonoda, *J. Geotechnical Engineering*, **109**, 832-844 (1983)
37. M.S. Kuczma and R. Switka, *Computers and Structures*, **34**, 125-136 (1990)
38. W.E. Boyce and R.C. DiPrima, *Elementary Differential Equations and Boundary Value Problems,* John Wiley and Sons, New York, 513-518 (1986)
39. R.J. Good and R.K. Gupta, *J. Adhesion*, **26**, 13-36 (1988)
40. T.L. Anderson, *Fracture Mechanics: Fundamentals and Applications*, CRC Press, Boca Raton, 314 (1995)
41. Y. Urahama, *J. Adhesion*, **31**, 47-58 (1989)
42. H. Obori, M. Takenaga, and A. Nakamura, *J. Adhesion*, **59**, 127-134 (1996)

APPENDIX A

The role of electrostatic attraction was considered during the investigation of the cling of thin polymeric films onto various substrate materials. Unlike the other mechanisms of adhesion, electrostatic attractive forces are capable of acting over relatively large distances. Because of this unique behavior, it may be possible to correlate any far-field effects observed during experimentation directly to the effect of electrostatic attractive forces acting between the polymer film and the substrate. Therefore, this study is presented which investigates the magnitude of electrostatic attractive forces which are functions of separation distance (between polymer film and substrate) and film-substrate width.

In order to determine the relationship between separation distance, film-substrate width, and electrostatic forces, it is necessary to determine the geometry of the system to be analyzed. For this work, a simplified system involving two parallel plates of equal dimensions is used, one plate representing the polymer film and the other plate representing the substrate. These plates are considered to be separated by a distance, r, as shown in Fig. A.1. For this study, it is assumed that each plate possesses uniform and equal but opposite charge.

The force of attraction between two equal but oppositely charged particles is given by the relation:

$$F(r) \propto \frac{1}{r^2}. \tag{A-1}$$

By considering the force of attraction between a particle located a distance r above a plate (of length, L and width, W), it is possible to integrate Eq. A-1 over the area of the plate to obtain the proportionality between the attractive forces and the geometry of the particular system (r, L, and W). With this equation, it is simply necessary to integrate once again over the same area to obtain the proportionality between the attractive forces and the geometry of the system for the case of two parallel plates, shown in Fig. A.1. This equation has the form

$$F(r) \propto \int_0^{WL}\int_{-Y}^{W-Y}\int_{-X}^{L-X} \frac{r}{\left(x^2+y^2+r^2\right)^{3/2}}\,dx\,dy\,dX\,dY, \tag{A-2}$$

where F is the electrostatic attractive force, L is the plate length, W is the plate width, r is the separation distance between the two plates, and the remaining variables (x, y, X, and

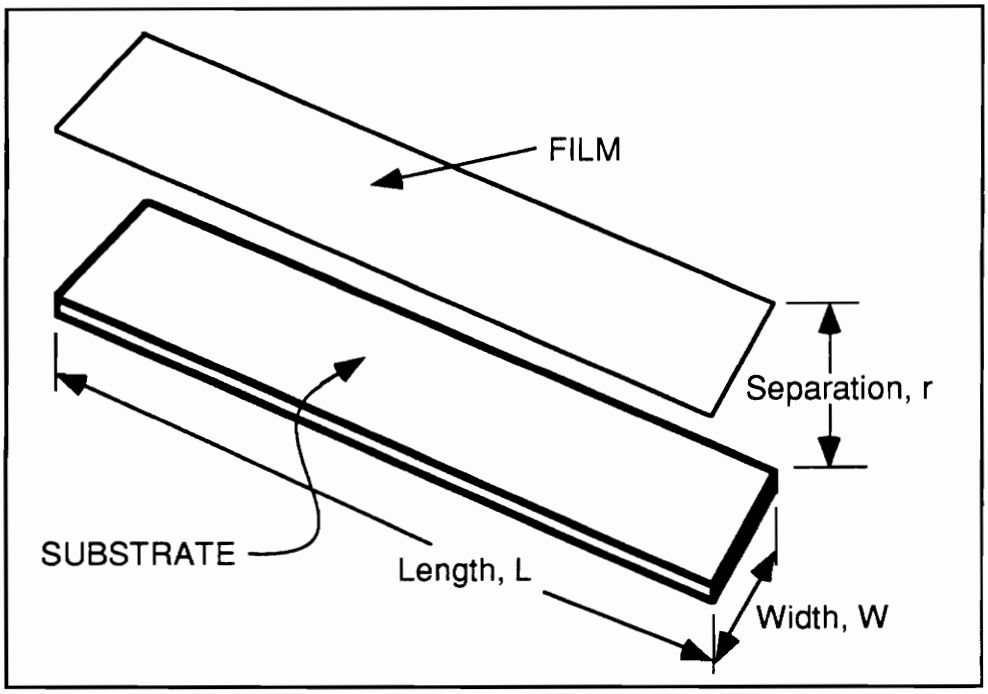

Figure A.1 - Geometry of the electrostatic attraction problem showing two parallel plates of equal length and width separated by a distance r.

Y) are variables of integration. The attractive force, F(r), in both Eqs. A-1 and A-2 may be written as the product of a function of the system geometry and a constant of proportionality, k. In subsequent results, the electrostatic attractive force will be given by F(r)/k.

The shape of the function F(r)/k is shown in Fig. A.2 for a plate of length 200 mm, width 10 mm, and separation distance 1 mm. The scale of the vertical axis, F(r)/k, is shown to range from 0 to 6. Two curves from this figure are used in Fig. A.3: the curve of F(r)/k along the length of the plate and the curve of F(r)/k along the width of the plate. Both curves are drawn along the center axes of the plate.

In Fig. A.3, these curves are shown for three different separation distances (r = 1 mm, 5 mm, and 10 mm) for the same size plate. The curves shown for the separation distance of 1 mm correspond to the curves identified in the three-dimensional plot of Fig. A.2. The solid curves represent the values of F(r)/k along the length, while the dashed curves represent the values of F(r)/k along the width of the plate. The magnitudes of these curves are shown to decrease as the separation distance increases. In other words, the magnitude of the attractive force decreases as the plates are separated. This is a function of the finite dimensions of the plates. In addition, the edge effects on the value of F(r)/k for changing separations are also shown.

To obtain the magnitude of the total attractive force given by F(r)/k, it is necessary to integrate the curve shown in Fig. A.2 for the area of the plate (Eq. A-2). These results are shown for four plates of different widths in Fig. A.4. In this figure, the value of F(r)/k acting over the entire plate as a function of separation distance is shown for plates of widths equal to 10 mm, 20 mm, 40 mm, and 80 mm. In each case, the value of F(r)/k drops as the separation distance increases, as is expected.

Of more interest is the nonlinear effect of variations in plate width on F(r)/k for increasing separation distance, r. To better see this effect, the results for F(r)/k shown in Fig. A.4 for the case of W = 10 mm are used to normalize the results for the other three cases. This is accomplished by dividing the value of F(r)/k for each case by the value of F(r)/k for W = 10 mm. This amount is normalized by the width of each case. Therefore, if there were no nonlinear effects due to changes in plate width, all four cases would fall on the same line, with a value of one. The non-liner factor for a given width, Φ_w, is defined a as

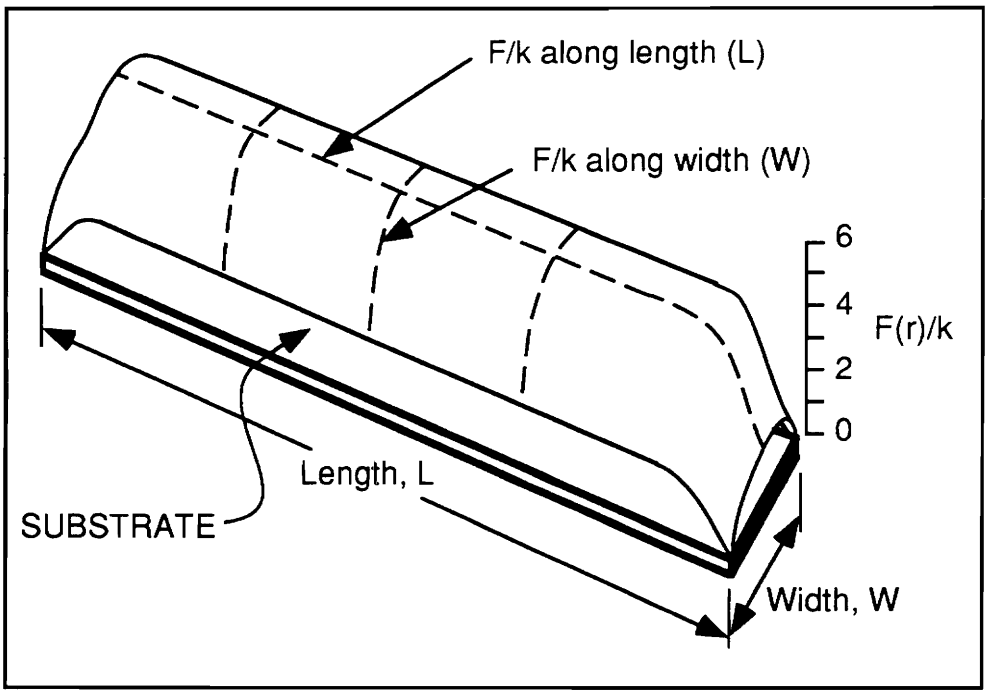

Figure A.2 - Distribution of F(r)/k for plate of width = 10 mm, length = 200 mm, and separation distance = 1 mm.

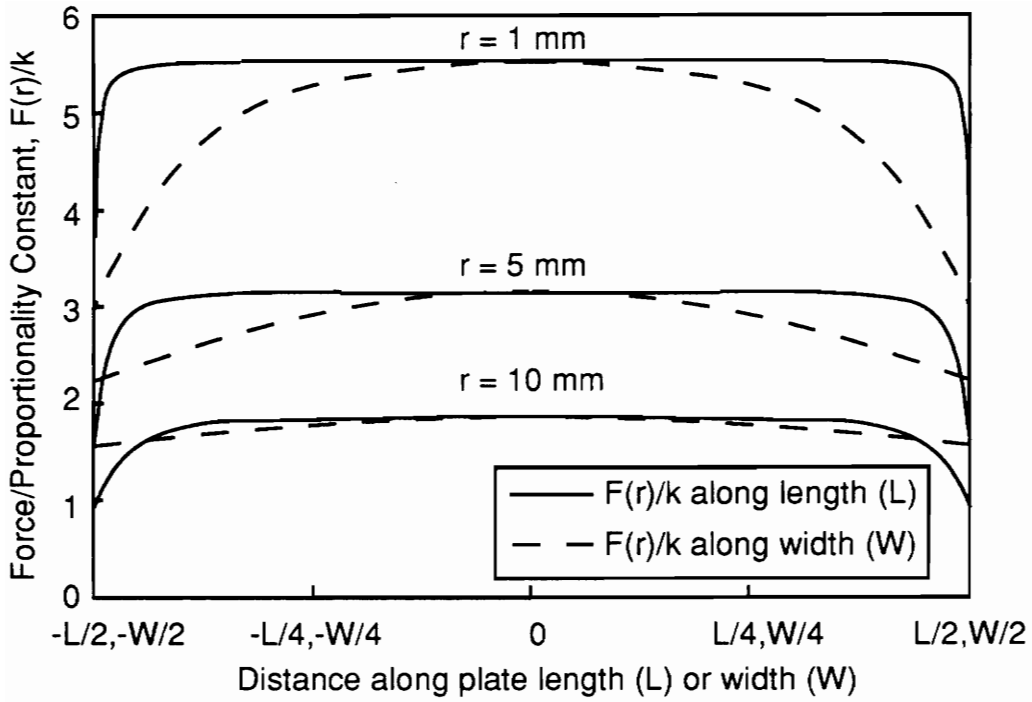

Figure A.3 - F(r)/k for plate of width = 10 mm at three separation distances, r.

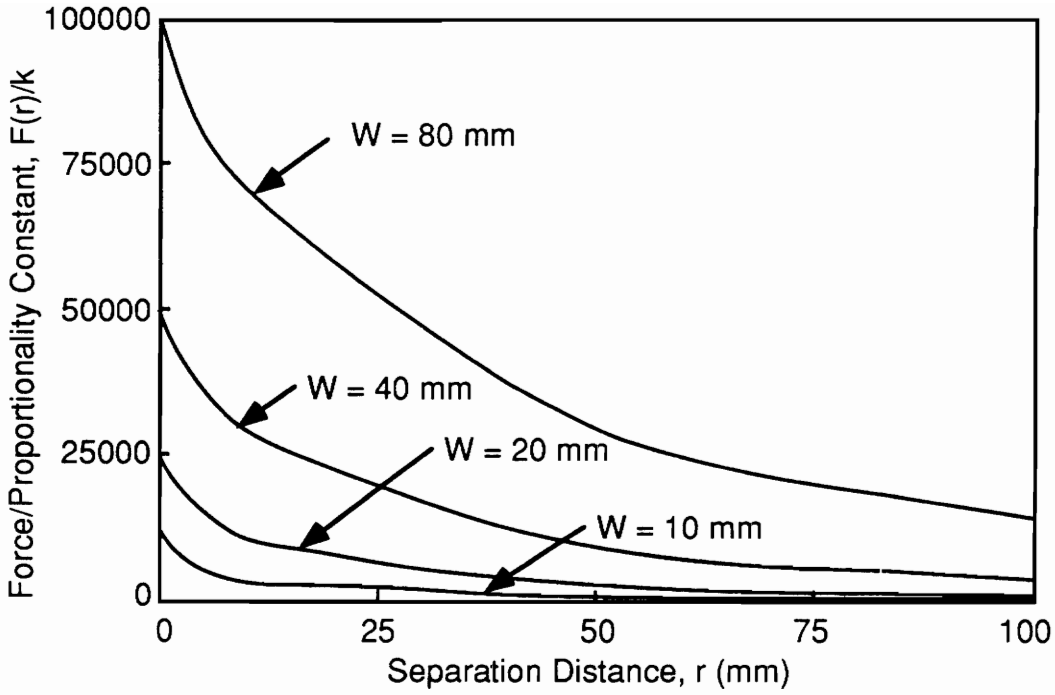

Figure A.4 - F(r)/k as a function of separation distance for four plates.

$$\Phi_W = \frac{\left[\frac{F(r)}{k}\right]_W}{\left[\frac{F(r)}{k}\right]_{W=10mm}} \left(\frac{W}{10mm}\right) \qquad \text{(A-3)}$$

The results from this analysis are shown in Fig. A.5. In this figure, the four cases are again shown by their widths. Since the case of W = 10 mm was used for normalization of the remaining curves, its value is always one. The other cases show increasing nonlinear effects as both separation distance and plate width increase. As an example, the plate area for the case of W = 80 mm is eight times as large as the area of the case for W = 10 mm. At a separation distance approaching 0 mm, this means the attractive force is also eight times larger for the case of W = 80 mm ($\approx$ 1 x 8). But, for a separation distance of 100 mm, the attractive force is over 56 times as large ($\approx$ 7 x 8).

Due to the finite size of these plates, electrostatic attractive forces are shown to exhibit nonlinear behavior for increasing plate size and increasing separation distance. Therefore, any nonlinear increases in observed adhesion strength with increased film-substrate width may be correlated to the effects of electrostatic attraction. Of course, since this effect becomes larger as separation distance increases while the magnitude of the attractive forces decreases as separation distance increases, it may not be possible to experimentally observe this phenomenon.

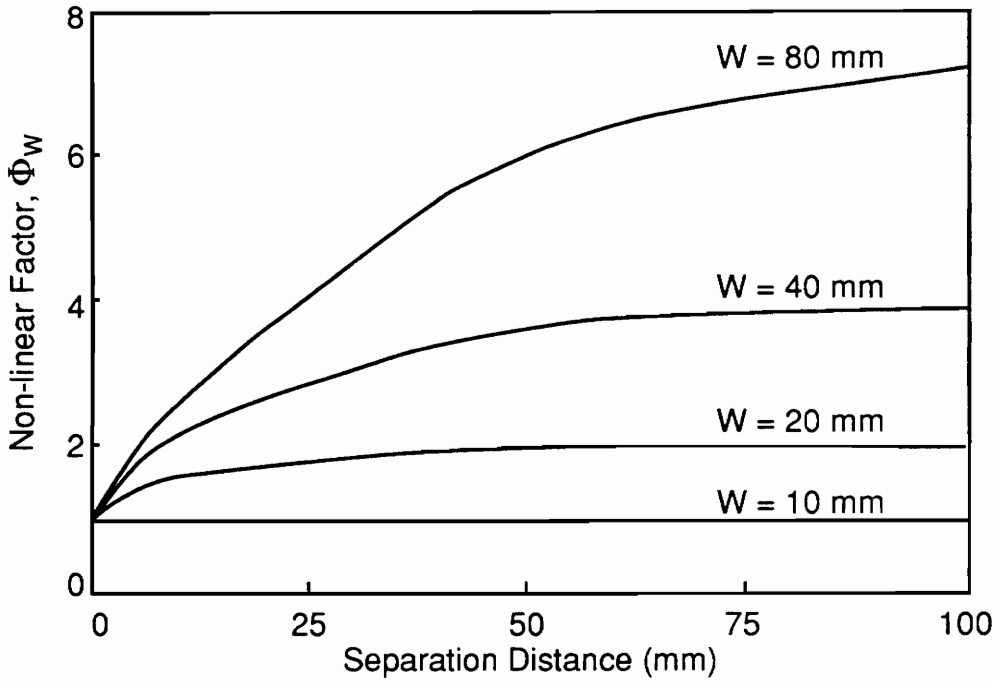

Figure A.5 - Non-linear factors for four plates showing non-linear effect of plate width for increasing separation distance, r.

APPENDIX B

Although the Maxwell fluid is used to represent the viscoelastic behav ... adhesive in the beam on a viscoelastic foundation analysis, the derivation of that solution is quite similar when modeling the adhesive with the three-parameter solid element. Therefore, the fundamental relations of the three-parameter solid model as well as the basics of the derivation of the beam on a viscoelastic solution are presented.

The three parameter solid element is shown in Fig. B.1. It consists of a Kelvin element in series with a Hookean spring. Analogous to Eqs. 3-7 and 3-8, the following equations represent the governing differential equation and the relaxation modulus:

$$\sigma + \left(\frac{\eta}{E_0 + E_1}\right)\dot{\sigma} = \left(\frac{E_0 E_1}{E_0 + E_1}\right)\varepsilon + \left(\frac{E_0 \eta}{E_0 + E_1}\right)\dot{\varepsilon} \quad \text{and} \tag{B-1}$$

$$Y(t) = E_0 e^{-\frac{E_0 + E_1}{\eta}t} + \frac{E_0 E_1}{E_0 + E_1}\left(1 - e^{-\frac{E_0 + E_1}{\eta}t}\right). \tag{B-2}$$

An analogous derivation to that presented in Section 3.3 may be used to model a linear elastic beam on a viscoelastic foundation represented as a three-parameter solid. In this case, the initial partial differential equation is represented by

$$u_{xxxx,t} + \alpha u_{xxxx} + \beta u_t + \gamma u = 0 \tag{B-3}$$

where

$$\alpha = \frac{E_o + E_1}{\eta},$$

$$\beta = \left(\frac{w}{h}\right)\frac{E_o}{EI}, \text{ and}$$

$$\gamma = \left(\frac{w}{h}\right)\frac{E_o E_1}{EI\eta}.$$

Therefore, by applying similar methods as were used to obtain Eq. 3-26, it is possible to write an analogous equation for the constant, μ,

$$\mu^4 = \frac{\beta\nu - \gamma}{\alpha - \nu}. \tag{B-4}$$

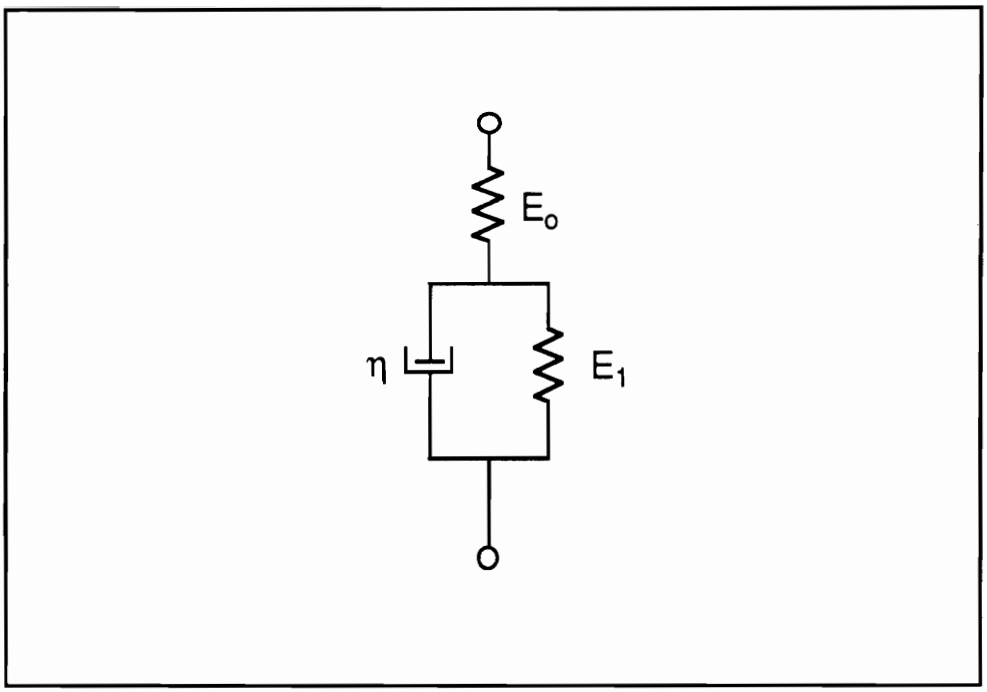

Figure B.1 - Schematic of the three-parameter solid element.

This leads to the identical form of the solution to the partial differential equation as was given by Eq. 3-35. As before, if the right-hand side of Eq. B-4 is less than zero, only the trivial solution satisfies the boundary conditions. The trivial solution is identical for both cases of the right-hand side of Eq. B-4 being greater than zero and less than zero.

APPENDIX C

Optimization of the bond geometry is one potential use of the beam on elastic foundation solution which was presented in Section 3.2. By assuming linear elastic behavior of the adhesive, the stress distribution along the bond line may be obtained from the beam deflection. By utilizing the solution for multiple curvature mismatch systems, it is possible to determine the effect of varying one or more geometric parameters which describe the bonded system. In other words, it is possible to determine the optimal bond geometry to minimize stress at critical points within the adhesive bond.

In this work, a simple example is shown to demonstrate the optimization technique. Consider an adhesive system as shown in Fig. C.1. An initially flat adherend is bonded to a rigid substrate with three distinct regions of curvature mismatch between the adherend and the substrate. The substrate consists of a long region of zero curvature mismatch followed by a rounded corner of radius, ρ. The third region is a flat land which follows the curved edge. The radius of the corner is studied to determine the optimal length to minimize stress within the bond. As a constraint on the acceptable values of ρ, it is required that the adherend must pass through both points A and B. Therefore, ρ can have a value no greater than 4 cm. In this case, there is also no flat land region. Theoretically, ρ may be as small as zero, although obviously the requirement that the adherend must remain in the elastic region would be violated.

Since the material properties of the adhesive and the adherend used in Section 3 are well known, the same materials will be considered for this sample case. The adherend is taken to have a width of 12.7 mm and a thickness of 0.2 mm. The adhesive has a width of 12.7 mm and a thickness of 1.14 mm. The initially flat region of the substrate is considered to be sufficiently long to neglect any end effects.

The multiple curvature mismatch solution as described in Section 3.2 is used to solve for the stress distribution at two points along the bond length as a function of the corner radius, ρ. The boundary conditions and matching conditions are given as follows:

$$u_{1_{xx}}(0) = u_{1_{xxx}}(0) = 0$$

$$u_{3_{xx}}(1-\rho) = u_{3_{xxx}}(1-\rho) = 0$$

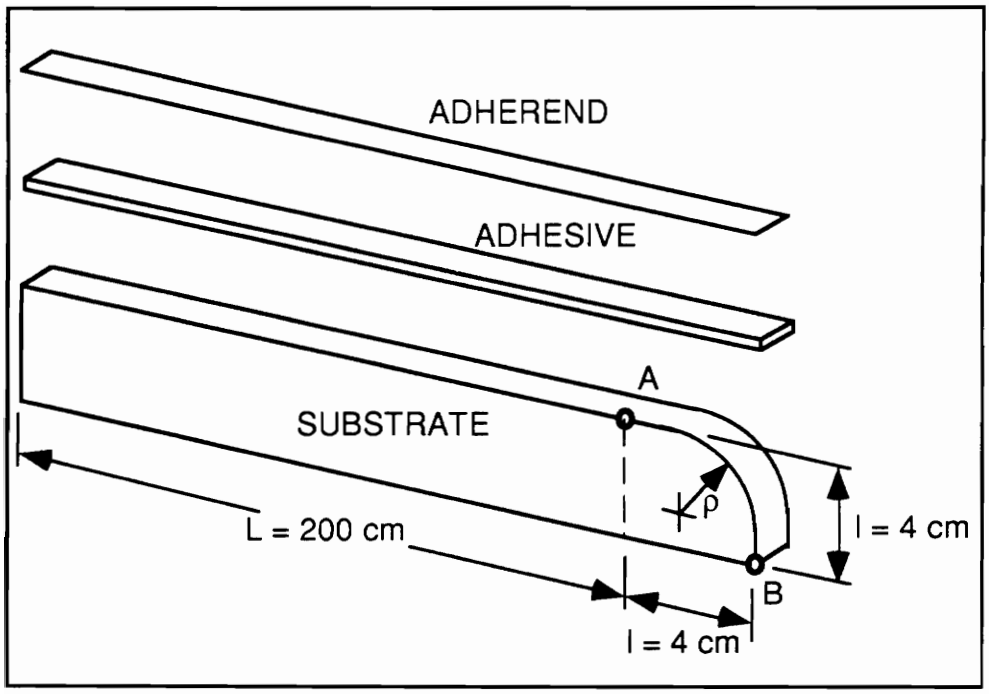

Figure C.1 - Geometry of the optimization problem.

$$u_1(L+l-\rho) = u_2(0) \qquad u_2\left(\frac{\pi\rho}{2}\right) = u_3(0)$$

$$u_{1_x}(L+l-\rho) = u_{2_x}(0) \qquad u_{2_x}\left(\frac{\pi\rho}{2}\right) = u_{3_x}(0)$$

$$u_{1_{xx}}(L+l-\rho) = u_{2_{xx}}(0) - \frac{1}{\rho} \qquad u_{2_{xx}}\left(\frac{\pi\rho}{2}\right) - \frac{1}{\rho} = u_{3_{xx}}(0)$$

$$u_{1_{xxx}}(L+l-\rho) = u_{2_{xxx}}(0) \qquad u_{2_{xxx}}\left(\frac{\pi\rho}{2}\right) = u_{3_{xxx}}(0)$$

where the geometric parameters are as shown in Fig. C.1. The deflection $u_1(x)$ is valid for $0 \leq x \leq (L+l-\rho)$, $u_2(x)$ is valid for $0 \leq x \leq (\pi\rho/2)$, and $u_3(x)$ is valid for $0 \leq x \leq (l-\rho)$. In other words, each corresponds to one of the discrete regions of curvature mismatch.

Stress curves are shown for four values of ρ in Fig. C.2. The right-hand side of the curves corresponds to the endpoint of the system, Point B. The two points considered in the stress analysis are the endpoint of the bond (Point B) and the point with the maximum tensile stress within the bond line away from the bond tip (this point, which varies, between values of 6 and 12 cm as shown in Fig. C.2).

The results of the solution of the multiple curvature mismatch region beam on elastic foundation analysis are shown in Fig. C.3. One curve corresponds to the stress as a function of ρ at the bond tip and the other curve corresponds to the maximum stress within the bond as a function of ρ. The values of ρ range from 0 to 4 cm. The dashed line at a stress equaling 170 kPa corresponds to the stress of the slider constant used within the Bingham model. The Bingham model predicts that no debonding of the adhesive will occur for stresses less than 170 kPa, assuming that an ultimate strain is used as the failure criterion.

The curve of the stress at the bond tip shows stress generally increasing as the radius, ρ, increases. This is due to the shortening of the flat land region at the bond end with increasing ρ. It is interesting to note that it is possible to obtain compressive stresses at the bond tip over a certain range of ρ (approximately 1.5 cm to 2.8 cm). The curve of the maximum stress within the bond acts in an opposite manner to the first curve. The

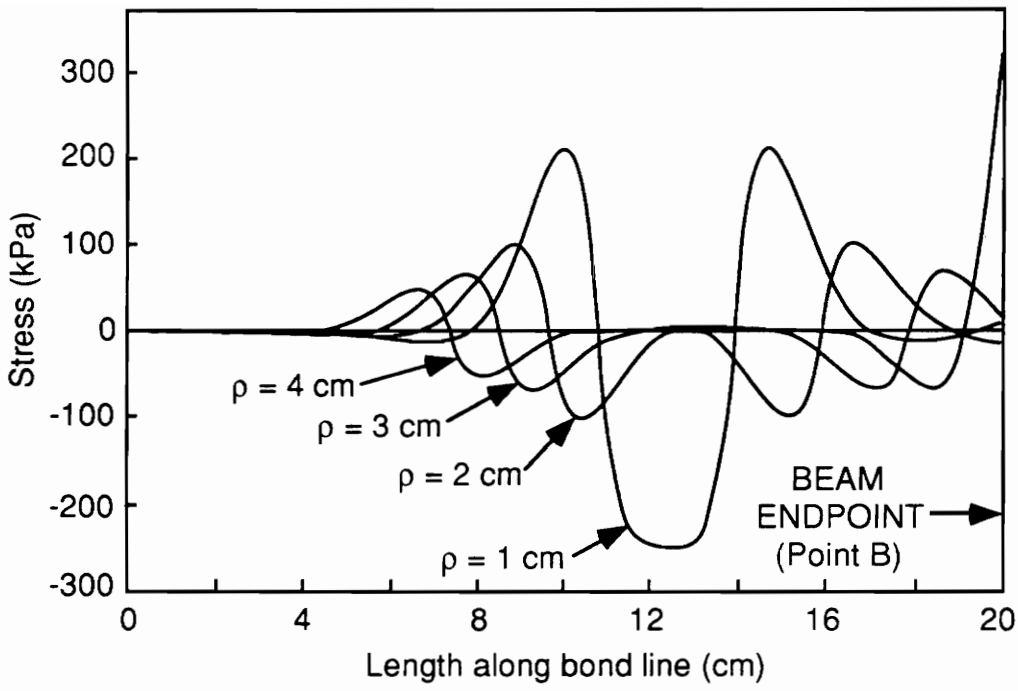

Figure C.2 - Stress distribution along bond line for four values of ρ (1 cm, 2 cm, 3 cm, and 4 cm).

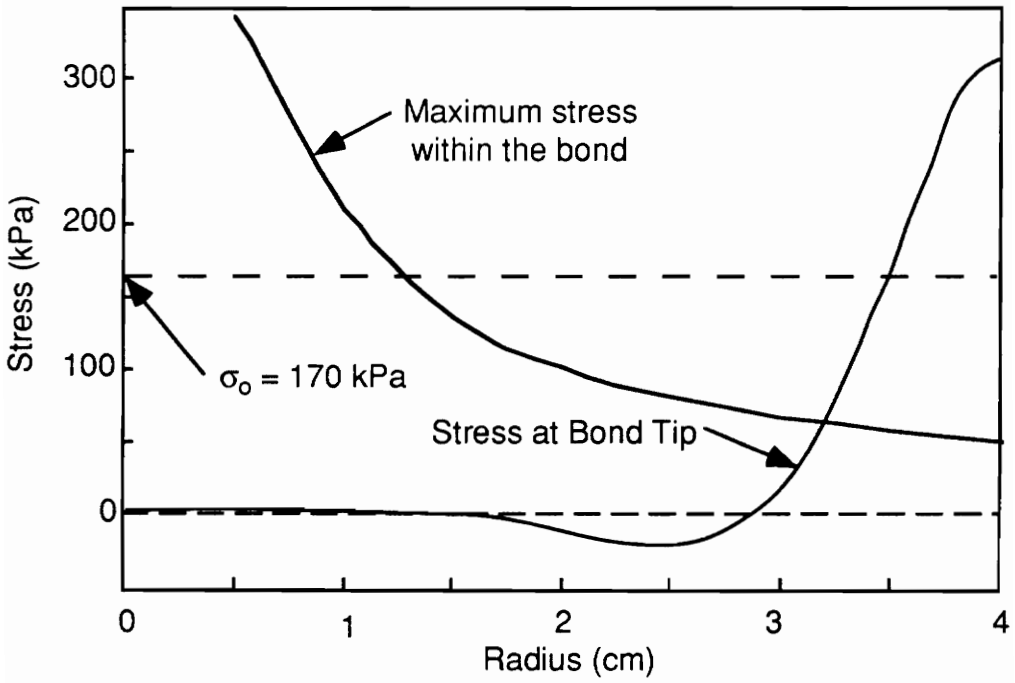

Figure C.3 - Optimization curves showing stress as a function of radius, ρ.

tensile stress within the bond is extremely high for small values of ρ. As the radius increases, the maximum stress within the bond away from the bond tip decreases.

This simple analysis suggests an optimal range of values for ρ which would produce the minimal tensile stress at the locations considered. Without a more rigorous failure criterion, it is impossible to draw additional conclusions from this work. It does appear that a geometry made up of a smaller radius and land region is more durable than a geometry of a larger radius with no land.

VITA

Charles Randow was born April 7, 1969 at Travis Air Force Base in California. After growing up in California, Japan, Virginia, and Chile, he began his undergraduate studies at Virginia Polytechnic Institute in 1987. After graduating in December 1992 with his Bachelor's degree in Engineering Science and Mechanics and working for the Montgomery County School Board, the author began graduate studies in Engineering Mechanics at the same university. The author will be working with Covington Research for Westvaco in Covington, Virginia.